The Controllable Delivery of Hydrophilic and Hydrophobic Drugs Using Starch Nanoparticle-based Clusters

By

E. Coulter Montague

A Thesis

Submitted to the School of Interdisciplinary Sciences

In Partial Fulfilment of the Requirements

For the Degree

Honours Bachelor of

Science

McMaster University

HONOURS BACHELOR OF SCIENCE (2020) McMaster University

School of Interdisciplinary Sciences Hamilton, Ontario

McMaster University, Hamilton, ON

TITLE: The Controllable Delivery of Hydrophilic and Hydrophobic Drugs Using Starch Nanoparticle-Based Clusters

AUTHOR: E. Coulter Montague

SUPERVISORS: Dr. Todd Hoare, Xiaoyun Li

Number of pages: xi, 86

Abstract

Despite the number of treatment methods currently available, cancer remains one of the leading causes of death in Canada and worldwide. It is therefore critical that new and more effective means of combating this disease be developed. Nanoparticles have been extensively investigated for their use in cancer diagnostics, imaging, and most critically in chemotherapeutic drug delivery. One such example is starch nanoparticles (SNPs), which can penetrate dense tumour cores based on their small size and have the capacity to be functionalized and loaded with different types of chemotherapeutic drugs. The size of SNPs, however, limits their potential to reach tumours due to their rapid clearance from the body. To address this challenge, we have fabricated electrostatic complexes – or nanoclusters – composed of cationic SNPs and anionic charge-switchable polymers that remain stable at physiological pH (7.4) and disassemble to release the highly penetrable SNPs when exposed to the acidic (6.5) microenvironment associated with tumours. Furthermore, recent research has indicated that the administration of certain combinations of chemotherapeutic agents can increase the efficacy of targeted cancer therapy while reducing the necessary dose to achieve remission. One example of this is the administration of the relatively hydrophobic EGFR inhibitor erlotinib (Erl), which can synergize cancer cell apoptosis with the more hydrophilic DNA damaging agent doxorubicin (Dox). Here, we reveal the ability to engineer two functionalized SNP variants capable of loading either Dox or Erl that can subsequently be used in nanocluster formation to deliver synergistic antitumour therapy *in vitro* and *in vivo*. Though drug loading and dual SNP carrying nanocluster formation remain to be assessed, SNP variant synthesis is an important step towards generating multi-drug delivering nanoclusters.

Acknowledgments

I would first like to thank my supervisor Dr. Todd Hoare for his faith, generosity, and mentorship during the course of this project and my previous work in his lab; and Xiaoyun Li for her guidance and support over the last year and a half. I would also like to thank all members of the Hoare Lab for their time and effort training me, and their meaningful discussions during our meetings. Not only have I gained a wealth of knowledge surrounding the research and applications of nanoparticles, but I have also been exposed to an incredible team of researchers who strive tirelessly towards the advancement of scientific exploration and application.

Thank you to the iTeach team and the Integrated Science cohort of 2020 for providing me with the opportunity to learn in such an interdisciplinary environment, and to pursue my passion for research; this has truly been a life changing experience.

Finally, I would like to thank my family and friends for standing by me over the course of my research, and during my entire undergraduate degree. I would not be where I am today without all of you.

Table of Contents

List of Illustrations and Diagrams

List of Abbreviations and Symbols

% w/v	Percent weight by volume
2D	Two-dimensional
3D	Three-dimensional
4T1	Breast cancer cells of the 4T1 cell line
AA	Acrylic acid
ADH	Adipic dihydrazide
AIBMe	2,2-azobisisobutryic acid dimethyl ester
Ald-SNPs	Aldehyde-functionalized starch nanoparticles
APTES	3-aminopropyltriethoxysilane
AuNPs	Gold nanoparticles
BT-20	A breast cancer cell line
DLS	Dynamic light scattering
DMA	2,3-dimethylmaleic anhydride
DMEM	Dulbecco's modified Eagle's medium
DMF	N,N-dimethylformamide
DNA	Deoxyribonucleic acid
Dox	Doxorubicin
EDC	1-(3-dimethylaminopropyl)-carbodiimide hydrochloride
EDTA	Ethylenediamine tetraacetic acid
EGFR	Epidermal growth factor receptor
EPR	Enhanced permeability and retention
Erl	Erlotinib
FBS	Fetal bovine serum
GPC	Gel permeation chromatography
HCl	Hydrochloric acid
HHG_2C_{18}-L	A pH-sensitive lipid bilayer composed of 1,5-dioctadecyl-L-glutamyl 2-histidyl-hexahydrobenzoic acid used in nanoparticles
HPLC	High-performance liquid chromatography
ICP-MS	Inductively coupled plasma-mass spectroscopy
IV	Intravenous

M-HHG$_2$C$_{18}$-L(E + D)	Amino-functionalized mesoporous silica nanoparticles loaded with doxorubicin and erlotinib
MMT	3-(4,5-dimethylthiazol-2-yl)-2,5-diphenyltetrazolium bromide
MMTV-PyMT	Breast cancer metastasis model
Mn	Number-average molecular weight
mol	Amount of a substance (6.023 x 10^{23} particles)
Mol%	Mole fraction
MQW	Millipore Milli-Q grade distilled deionized water
MS	Mass spectroscopy
Ms-DDs	Multistage drug delivery systems
MSN-NH$_2$	Amino-functionalized mesoporous silica nanoparticles
Mw	Midpoint of the distribution in terms of the number of molecules
NaCl	Sodium chloride
NaHCO$_3$	Sodium bicarbonate
NaIO$_4$	Sodium periodate
NaOH	Sodium hydroxide
NPs	Nanoparticles
OctSAn	2-Octen-1-ylsuccinic anhydride
OctSAn-SNPs	Octenyl succinic anhydride-functionalized starch nanoparticles
OEGMA$_{475}$	Oligoethylene glycol methacrylate
PBS	Phosphate buffer saline
PEG	Polyethylene glycol
pHe	Extracellular pH
pHi	Intracellular pH
POEGMA	Poly(oligoethylene glycol methacrylate)
POEGMA-AA	Poly(oligoethylene glycol methacrylate) functionalized with acrylic acid
POEGMA-Hyd-DMA	Poly(oligoethylene glycol methacrylate) functionalized with hydrazide and 2,3-dimethylmaleic anhydride
PS	Penicillin streptomycin
RES	reticuloendothelial system
RPM	Rotations per minute
SAn	Succinic anhydride

SAn-SNPs	Succinic anhydride-functionalized starch nanoparticles
SNPs	Starch nanoparticles
TEM	Transmission electron microscopy
TGA	Thioglycolic acid
UV	Ultraviolet light
wt%	Percentage by mass

Thesis Outline

This thesis has been divided into three parts. Part 1 consists of a literature review discussing the use of nanoparticles for drug delivery and general challenges associated with this method, approaches to designing nanoparticle delivery systems, various types of nanoparticles that have been investigated as well as their strengths and weaknesses, nanoparticle-based multi-drug therapy, and two types of *in vitro* experiments that can be used to assess the efficacy of chemotherapeutics and nanoparticle-based drug delivery. Part 2 of this thesis contains a report of the research conducted thus far and includes a project introduction, materials and methods, results, a discussion, and a conclusion based on current findings. Part 3 of this report builds upon Part 2, discussing the future directions of this research in more detail. This section provides additional methods and protocols for experiments to be conducted moving forward with this research in addition to containing sections outlining expected results from these experiments as well as addressing some of the potential problems that may arise during dual SNP carrying nanocluster design and evaluation.

PART 1: LITERATURE REVIEW

1.1 Introduction

Modern medicine is capable of a number of anti-tumour therapeutic approaches, including surgery, chemotherapy, radiotherapy, and hormone therapy (Bahrami et al., 2017). Even so, cancer remains one of the leading causes of death worldwide according to the World Health Organization (2018). It is predicted that in 2020 there will be 225,800 new cancer cases, and 83,300 cancer related deaths in Canada alone (Canadian Cancer Statistics, 2019). With such high incidence and mortality rates, it is critical that novel and more effective treatment methods be developed to treat cancer. One mode of treatment currently under intensive investigation is the use of nanoparticles (NPs) capable of delivering chemotherapeutic drugs directly to tumours and within cancer cells (L. Li et al., 2015; Y. Li et al., 2015).

NP drug delivery systems have been extensively researched since 1986, when the enhanced permeability and retention (EPR) effect was first described (Matsumura and Maeda, 1986; Egusquiaguirre et al., 2012). This ultimately led to the emergence of nanomedicine, described as the application of nanotechnology to medicine and healthcare (Matsumura and Maeda, 1986; Wagner et al., 2006). Despite the EPR effect serving as the rationale for many drug-carrier designs – costing billions of dollars over several decades – it has been shown to only marginally improve experimental drug delivery (Nichols and Bae, 2014; Danhier, 2016). In spite of this, there are currently a number of nanoparticle therapeutics as well as imaging agents and technologies that have been approved for clinical use largely based on their advantages over non-formulated and free drug administration, such as their ability to deliver therapeutics and treat areas of the body that other delivery systems cannot reach, to reduce systemic toxicity of the

drugs administered, and to reduce the overall dosage necessary for achieving therapeutic drug concentrations in a target area (Anselmo and Mitragotri, 2016).

To serve as an effective method of cancer drug delivery, NPs must overcome several physiological barriers that impose conflicting requirements on both their size and charge. These barriers limit a NP's ability to remain in the blood during circulation, accumulate at the site of action, and penetrate a tumour to deliver a chemotherapeutic agent (B. Chen et al., 2017). To accommodate for the variation in requirements for a NPs size and charge at different points in the delivery process, many researchers are currently working to design particles capable of undergoing novel surface or structural changes in response to certain stimuli to enhance NP-drug tolerability, circulation half-life, and therapeutic efficacy (Gao, Chan and Farokhzad, 2010; Sperling and Parak, 2010). Specifically, it has been found that NPs capable of undergoing either a physically (temperature, electric field, magnetic field, and ultrasound) or chemically (pH, ionic strength, redox potential, and enzymatic activity) stimulated change in response to the tumour microenvironment or an external stimulus when at the site of action display enhanced efficacy in cancer treatment (Gao, Chan and Farokhzad, 2010).

1.2 Physiological Barriers to Nanoparticle Drug Delivery

1.2.1 Nanoparticle Circulation

In order for NPs to remain in the bloodstream and avoid rapid renal excretion, aggregating with plasma proteins and being eliminated by monocytes or phagocytes of the reticuloendothelial system (RES), and off-target cell interactions, their surface must be negatively charged or neutral (Ma et al., 2005; Hatakeyama et al., 2006; L. Li et al., 2015; B. Chen et al., 2017). Certain

surface modifications, such as the attachment of polyethylene glycol (PEGylation) also support a NP's evasion of removal (in this case, by the RES) (Li and Huang, 2009). The kidney's filtration system – glomeruli containing three layers with varying pore sizes – imposes an effective NP minimum size cutoff for their overall structure of 10 nanometres (nm). (Nie, 2010; Soo Choi et al., 2007). As well, NPs with a diameter greater than 200 nm activate the body's complement filtration system – a component of the body's innate immune response consisting of a series of proteins that exist in blood plasma or on cell surfaces as inactive precursors (zymogens) – causing them to be removed from the bloodstream and accumulate in the liver and spleen (Faraji and Wipf, 2009; de Barros et al., 2012; Nesargikar, Spiller, and Chavez, 2012; Kulkarni and Feng, 2013). While 10 and 200 nm represent the absolute size boundaries for NPs to be capable of circulating throughout the body without being at risk of filtration or removal, studies suggest that a maximum size limit of 100-150 nm allows them to circulate longer while concurrently avoiding substantial elimination (Moghimi, Hunter, and Andresen, 2012; Hoshyar, Gray, Han and Bao, 2016).

1.2.2 Nanoparticle Accumulation in Tumour Tissues

Another challenge with the use of chemotherapeutic carrying NPs is ensuring their accumulation at the site of a tumour. A number of studies have shown that NPs of around 100 nm accumulate well at tumours – believed to be caused by the EPR effect stemming from the 'leaky' vasculature associated with tumours (Matsumura and Maeda, 1986; O'Brien et al., 2004; Cabral et al., 2011; Jinqiang Wang et al., 2015). Further investigation into the means through which NPs can accumulate in tumours, however, has revealed an alternative mechanism involving the use of a

metabolically active transport process across endothelial cells – transcytosis – is likely responsible for this phenomenon (Sindhwani et al., 2020).

1.2.2.1 Angiogenesis

Angiogenesis under normal conditions is the process in which endogenous local or systemic chemical signals induce the formation of new blood vessels or the repair of damaged vessels by endothelial and smooth muscle cell growth, migration, and differentiation (Risau, 1997; Carmeliet, 2000; Rajabi and Mousa, 2017). This ensures the movement of oxygen and essential nutrients to newly forming or reforming tissue (Egusquiaguirre et al., 2012; Rajabi and Mousa, 2017).

1.2.2.2 Tumour Tissues and the Enhanced Permeability and Retention Effect

Cancer cells divide at a rapid and uncontrolled rate compared to most healthy cells leading to the reduction of oxygen and nutrient flow into a tumour and thus the formation of hypoxic conditions (Lammers, et al., 2012). To accommodate for these conditions, cancer cells overexpress pro-angiogenic growth factors, key among them being vascular endothelial growth factor. Such abnormal proliferation of endothelial cells and growth of the vascular network, however, generates disorganized vessels possessing incomplete endothelial lining with relatively large pores of 0.1–3 micrometres (μm) in diameter, leading to significantly higher vascular permeability and hydraulic conductivity (McDonald, Thurston, and Baluk, 1999; Jain and Stylianopoulos, 2010; Danquah, Zhang, and Mahato, 2011; Azzi, Hebda, and Gavard, 2013). This vascular permeability may subsequently drive tumour-induced angiogenesis, blood flow disturbances, inflammatory cell infiltration, and tumour cell extravasation. In addition to generating leaky vasculature, cancer cell proliferation is also capable of

causing the collapse of intratumoural lymphatic vessels by compression, leaving only outlying tumour lymphatic vessels functional (Padera et al., 2002). This impaired lymphatic drainage coupled with the leaky vasculature from abnormal growth is responsible for the so-called EPR effect.

1.2.2.3 Nanoparticle Accumulation in Tumours Based on the Enhanced Permeability and Retention Effect

Despite the promise that the EPR effect initially presented for supporting small macromolecules and NPs to accumulate in tumours (Matsumura and Maeda, 1986; O'Brien et al., 2004; Cabral et al., 2011; Jie Wang et al., 2015), resultant drug delivery was subsequently observed to be limited since the rate of leakage from the vessels was slow and drugs released at this stage were susceptible to being excreted or metabolized during the time it takes for the accumulation to reach therapeutic levels (Prabhakar et al., 2013). Quantitative analysis performed by Prabhakar et al. (2013) has also indicated that the EPR effect provides a less than two-fold increase in drug delivery to tumours compared to other organs in the body in mice. While this is insufficient in most cases for achieving therapeutic levels within a tumour, side effects are still often reduced in normal tissues which lack EPR (O'Brien et al., 2004).

Failure of the EPR effect to result in significant increases in therapeutic delivery to tumours *in vivo* must be considered in the context of experiments themselves. The EPR effect described by Matsumura and Maeda (1986) was observed in mice, where tumours grow rapidly, which leads to blood vessels not developing properly and consequently being leaky with endothelial cells presenting many fenestrations (Lammers, et al., 2012). In humans, however, tumour growth is less rapid, and fewer tumour vessels form endothelial gaps and become leaky (Jain and

Stylianopoulos, 2010). As a result, there is a heterogeneous distribution of pore sizes across tumours, and thus of NP extravasation between tumours, and limited benefit of the EPR effect in clinical NP-based drug delivery.

1.2.2.4 Nanoparticle Accumulation in Tumours Based on Trans-endothelial Transport

In an effort to determine the mechanism for NP accumulation in human tumours, Sindhwani et al. (2020) compared the presence of epithelial gaps – responsible for passive accumulation – and structures related to trans-endothelial pathways – responsible for active accumulation – in several tumour models. The authors then examined the extent to which each entry method independently contributes to NP accumulation using a computer model and multiple *in vivo* analyses. These aforementioned trans-endothelial pathways are related to transcytosis, which involves endothelial cells rearranging their cytoskeletons and cell membranes to generate vesiculo-vacuolar organelles (vacuoles) that can trap and transport nutrients and macromolecules by forming diaphragms called fenestrae or move directly through the cytoplasm following endocytosis (Schnitzer, 1992; Feng et al., 1997; Neal and Michel, 1997; Thurston et al., 1998; Feng et al., 1999; McDonald, 1999; Michel and Neal, 1999; Nagy et al., 2006; Oh et al., 2014).

To assess the presence of endothelial gaps, Sindhwani et al. (2020) first used transmission electron microscopy (TEM) and three-dimensional (3D) microscopy to determine their frequency, or density, in tumour blood vessels. Three different tumour models were selected, including the U87-MG glioblastoma xenograft model due to its prior use to establish gaps as a potential route for extravasation (Hobbs et al., 1998; Jain, 1999) as well as three other tumour models selected for their relevance to human tumours: slower growing syngeneic (4T1) breast

cancer, genetically engineered (MMTV-PyMT) breast cancer, and patient-derived xenograft breast cancer. Researchers calculated the average overall gap coverage to be 0.048% of the blood vessel surface area, or 500 gaps/square millimeter (mm^2) (an average of 2.8 gaps/mm with respect to the total major axis length and 1.1 gaps/mm with respect to the total vessel perimeter). Interestingly, only 7 out of 26 gaps were inter-endothelial, the remaining 19 being transcellular channels. This data was used to develop a mathematical modelling built using 3D images of tumour vasculature, results from which were compared to *in vivo* accumulation of 50 nm PEGylated gold NPs (AuNPs) using inductively coupled plasma-mass spectrometry (ICP-MS). Here it was found that simulated NP accumulation in tumours was approximately 40-fold less than the ICP-MS measurements, and that a gap density of almost 30,000 gaps/mm^2 would be required to explain the measured accumulation *in vivo*. This indicated that such vascular gaps alone could not account for, and are not in fact a significant contributor to, NP accumulation in tumours.

Sindhwani et al. (2020) then sought to determine the density of trans-endothelial pathways in the same tumour models assessed for gap density. Using TEM, it was found that fenestrae had an average frequency of 60 fenestrae/mm with respect to the total major axis length and 24 fenestrae/mm with respect to the total vessel perimeter. Vacuoles occurred at a frequency of 290 vacuoles/mm with respect to the total major axis length and 111 vacuoles/mm with respect to the total vessel perimeter. Together these structures occurred much more frequently than endothelial gaps. TEM of *in vivo* models after administering various sizes of AuNPs (15, 50, and 100 nm) also revealed NP presence in vesicles and cytoplasm and along the membrane of the

endothelial cells of tumour vessels, providing evidence that NPs could indeed enter and traverse endothelial cells in a transcytosis-based manner.

Finally, to directly compare NP accumulation in tumours resulting from both endothelial gaps and trans-endothelial pathways, Sindhwani et al. (2020) developed a 'zombie' model, where tumour-bearing mice were perfused with a fixative to deactivate any cellular activity while preserving vessel architecture. This allowed researchers to separate the contribution to NP accumulation of passive gap diffusion and active transendothelial transport to determine which was the dominant mechanism, since here the active mechanism was deactivated. ICP-MS analyses revealed that endothelial gaps only accounted for the accumulation of up to 3% and 25% of AuNPs of 50 and 100 nm *in vivo* respectively compared to control mice, indicating that active transport was a major contributor to NP accumulation in tumour tissues. This finding was further confirmed using spatial analyses evaluating the endothelial features that were closest to extravasated NPs in both the zombie and control mice and testing for correlations between the location of these NPs with either active transendothelial or passive gap-based transport pathways. This component of the investigation revealed that correlation between extravasated AuNPs and endothelial features was strongest with tight junctions, which was speculated to be the result of the regions surrounding tight junctions possessing the thinnest part of the lumen and thus allowing for NP transport through invaginations that form vesicles and fenestrae (Dvorak et al., 1988; Michel and Neal, 1999; Feng et al., 2002; Sindhwani et al., 2020). Extravasated AuNPs also significantly correlated with vesicles and other components of active transendothelial transport pathways, suggesting they most likely followed one of these routes as they entered the tumour microenvironment; and did not correlate significantly with any type of

endothelial gaps. Ultimately this study provided evidence that a metabolically active transport process across endothelial cells was responsible for heightened NP accumulation in tumour tissues. This represented a major paradigm shift in NP research away from the belief that passive gap-based transport pathways were responsible for the phenomenon of NP accumulation in tumours – a viewpoint that was held for over 30 years. With that said however, the extent to which this active transport mechanism and others contribute to NP accumulation in tumours must be assessed for each type of NP proposed for use in chemotherapeutic drug delivery. This will allow researchers to advance their specific designs and tailor experimental research towards enhancing their suitable clinical application and efficacy.

1.2.3 Tumour Penetration

Once NPs have accumulated at the site of a tumour, they must then penetrate it in order to effectively deliver their chemotherapeutic drug. The size of the NP that best allows for tumour penetration, however, is much smaller than that for accumulation. Tumor core penetration, and by extension high therapeutic efficacy, is achieved by NPs of 30 nm or less due to the extremely small interstitial space between tumour cells (Cabral et al., 2011; Jie Wang et al., 2015). As well, while possessing a negative charge or remaining neutral supports circulation in the bloodstream, positively charged NPs electrostatically bind with negatively charged tumour cell membranes, leading to improved cellular uptake (Ma et al., 2005; Hatakeyama et al., 2006; L. Li et al., 2015; B. Chen et al., 2017).

1.3 Approaches to Designing Nanoparticle Drug Delivery Systems

1.3.1 Multistage Drug Delivery Systems

Multistage drug delivery systems (Ms-DDS) are designed around the use of NPs that demonstrate different characteristics and behaviors between systemic circulation and the external tumour microenvironment (B. Chen et al., 2017). Stimuli for Ms-DDS are divided into extracorporeal physical stimuli, the endogenous tumour microenvironment, and intracellular biological stimuli. These forms of stimulus have the potential to cause changes to NP size, charge, hydrophobicity, and even cause carrier degradation or disassembly. Here, the focus will be placed on the roles of the acidic tumour microenvironment, charge reversal, and size shrinkage.

1.3.2 Acidic Tumour Microenvironments

The pH of the extracellular tumour microenvironment (6.5-7.2) and intracellular endosomes and lysosomes (4.5-5.5) are the most common triggers for stimuli-responsive NP drug-delivery (Cardone, Casavola and Reshkin, 2005; B. Chen et al., 2017; W. Chen et al., 2017; Zhou et al., 2018). This is largely due to the universality of these characteristics in most solid tumours. The decrease from the physiological pH (7.4) in the region around the tumour is due to the Warburg effect, first proposed by Otto Warburg in the 1930s (Vander, 2009; L. Li et al., 2015). This phenomenon illustrates the increase in glucose uptake and aerobic glycolysis in cancer cells, leading to higher lactate production even under normoxic conditions (Gatenby and Gillies, 2004; He et al., 2013). pH-sensitive nanocarriers are capable of a number of physicochemical changes to their material structure and surface characteristics that can be based on chemical groups becoming ionized, chemical bond cleavage revealing buried functional groups, pH-sensitive

peptides, gas-generating systems, and pH-responsive polymers that may undergo structural degradation or disassembly (Gao, Chan and Farokhzad, 2010; B. Chen et al., 2017). Despite extensive research and verification, however, the exploitation of the acidic tumour microenvironment remains a challenge. In many instances the acidic pH is located away from blood vessels, meaning nanocarriers must penetrate the tumour to experience a stimulus, and that there is a limited response by pH-stimulated NPs in the perivascular regions of the tumour. In addition, the pH difference between normal and cancerous tissue may in some cases only differ slightly, preventing a sufficient nanocarrier response. This necessitates the design of more sensitive nanocarriers that can respond to these small pH variations, but still remain safe for systemic administration.

1.3.3 Nanoparticle Charge Reversal

The surface charge of NPs is another key factor that influences their stability, tumour targeting, and cellular uptake and is often manipulated to overcome the challenge of conflicting requirements for NP-based chemotherapeutic drug delivery (B. Chen et al., 2017). Research into this NP delivery mechanism has ultimately led to the creation of charge-switchable Ms-DDS, which possess a negative or neutral charge in the bloodstream but convert to being positively charged in the tumour microenvironment. This charge reversal is usually done through the inclusion of ionizable chemical groups or pH-cleavable chemical bonds (amide bonds between a hydrazide and dimethyl maleic anhydride for example) (B. Chen et al., 2017; Ooi et al., 2020). Charge reversal also supports lysosomal escape after cellular uptake allowing for enhanced intracellular drug delivery (B. Chen et al., 2017).

1.3.4 Nanoparticle Size Shrinkage

A critical aspect of NP chemotherapeutic drug delivery is tumour penetration (B. Chen et al., 2017). Physical resistance to NP distribution may be caused by a number of factors, including tumour heterogeneity (Denison and Bae, 2012; Junttila and de Sauvage, 2013), cross-linked extracellular matrix, aberrant tumour vessels (Miao, Lin and Huang, 2015), and abnormally elevated interstitial fluid pressure (Heldin et al., 2004). Two strategies have been devised to counter the issue of restricted distribution (B. Chen et al., 2017). One such method is the generation of NPs with size-changeable abilities. These systems are usually made up of large (~100 nm) 'mothership' carriers and encapsulated or bound small (~10 nm) 'babyship' carriers. These allow for the mothership carriers to remain stable during systemic delivery and accumulate in tumour tissues, as well as for the delivery of drugs into the deep regions of tumours after a stimulus, typically chemical in nature, causes the release of the babyship NPs.

A more frequently used approach to enhancing tumour penetration and NP drug delivery is referred to as 'tumour priming', where the microenvironment of the tumour is modulated (B. Chen et al., 2017). This may be done using cytotoxic drugs intended to decrease cell density (Alvarez et al., 2013; Jie Wang et al., 2015; Chen et al., 2016), hyperthermia therapy to improve vascular perfusion (Frazier and Ghandehari, 2015), or other methods that will allow for better NP penetration of the tumour (Fan et al., 2013; Kohli, Kivimäe, Tiffany and Szoka, 2014). Such tumour priming methods, however, are often used alongside other drug-loaded NPs, meaning a great effort is required to balance or determine multiple drug dosages, administration sequence, and inter-dose intervals (B. Chen et al., 2017). In addition, the separate administration of the

tumour priming system from the tumour-therapy system often results in poor compliance and higher overall toxicity.

1.4 Nanoparticle-based Multi-drug Therapy

1.4.1 Nanocarrier Synergistic Therapy

In order to enhance the efficacy of chemotherapy-based cancer treatment, researchers have begun to examine the effects that administering multiple drugs in succession or simultaneously has on the therapeutic potential of chemotherapy and drug delivery systems (Lee et al., 2012; Morton et al., 2014). While seeking to identify new strategies to enhance the initial chemoselectivity of triple-negative breast cancers, Lee et al. (2012) explored whether manipulating the interface between growth factor and deoxyribonucleic acid (DNA) damage signaling pathways in tumor cells could modulate the therapeutic response of this tumor type. Researchers were ultimately able to determine that pretreatment with epidermal growth factor receptor (EGFR) inhibitors, such as the hydrophobic drug erlotinib (Erl), can synergize with the apoptotic response of cancer cells to DNA-damaging chemotherapy, such as with the hydrophilic drug doxorubicin (Dox). This observed synergy is believed to have occurred through a ‘rewiring’ of oncogenic signaling networks and ‘unmasking’ of apoptotic pathways involving caspase-8, a member of the cysteine proteases that are implicated in apoptosis and cytokine processing (Barnhart, Alappat and Peter, 2003; Lee et al., 2012; Morton et al., 2014). It should be noted that while these findings indicate the possibility of increasing the efficacy of chemotherapeutic treatments, synergism between the EGFR inhibitors and DNA-damaging agents was observed to be both dose- and schedule-dependent (Lee et al., 2012). With regards to the time-dependency of drug administration, it has been found that when Erl is administered at least 4 hours prior to Dox,

the unmasking of suppressed proapoptotic pathways occurs, as seen in Figure 1. In order to maximize the synergistic effects of the combination chemotherapy, however, it has been found that there needs to be a specific time lag of 24 hours between the administration of each drug, also seen in Figure 1. Further, the enhanced sensitivity of cancer cells to Dox was observed to require sustained inhibition of EGFR, since it was the activity of the EGFR pathway rather than simply EGFR expression that determined whether time-staggered inhibition resulted in a synergistic cytotoxic effect. The different pharmacokinetic parameters of each drug, along with poor penetration and distribution in solid tumors, cause difficulties with their targeting to the same tumor cells and limit their adequacy as chemotherapeutic agents *in vivo* (Primeau et al., 2005; Huber et al., 2014). There also remain the issues of compliance, and toxicity when administering multiple drugs in sequence (B. Chen et al., 2017). Nevertheless, the findings from Lee et al. (2012) have spurred further research into the synergistic effect of EGFR inhibitors and cytotoxic drugs, a subject of growing interest in the field of nanomedicine involving NP-based drug delivery.

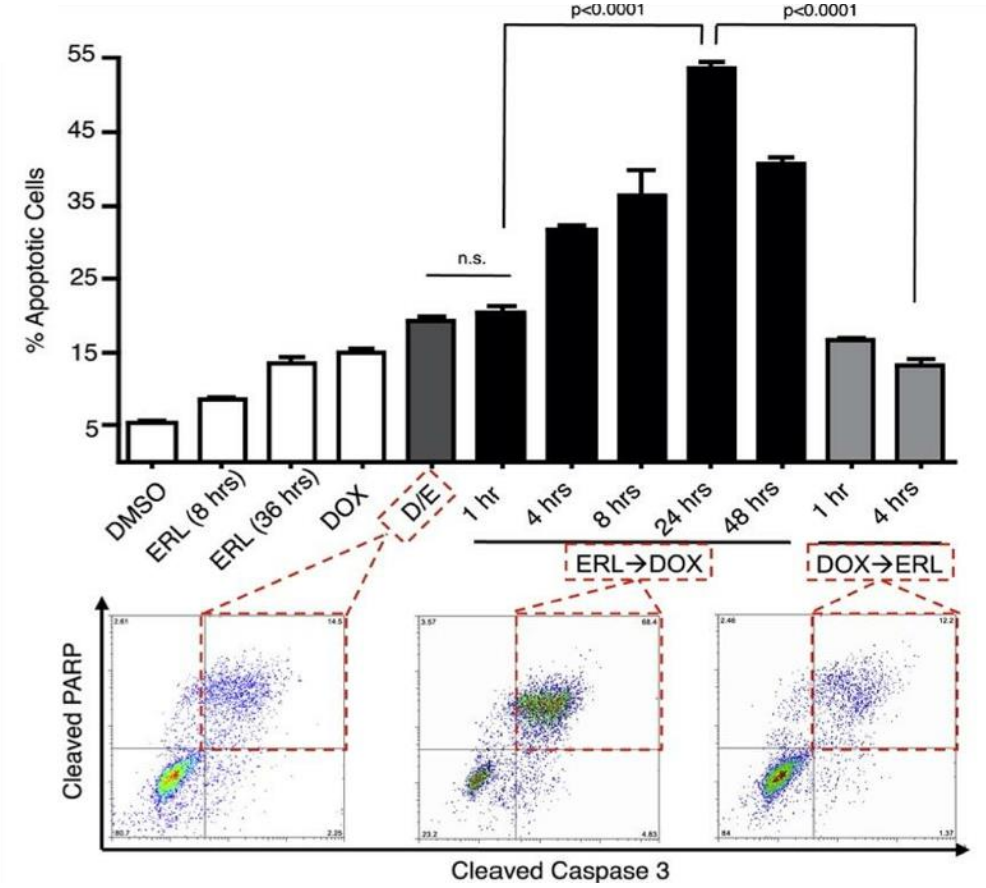

Figure 1: Apoptosis in BT-20 cells. Cleaved-caspase 3/cleaved-PARP double-positive cells were quantified using flow cytometry (bottom). In cells treated with DMSO, erlotinib (Erl), or doxorubicin (Dox), apoptosis measurements were performed 8 hr after drug exposure or at the indicated times. D/E, Erl→Dox, and Dox→Erl refer to Dox and Erl added at the same time, Erl given at the indicated times before Dox, and Dox given at the indicated times before Erl, respectively. For each, apoptotic measurements were made 8 hr after the addition of Dox. Erlotinib and doxorubicin were used at 10 μM. Mean values ±SD of three independent experiments, each performed in duplicate, are shown (top) (Lee et al., 2012).

1.4.2 Multi-drug Delivery Systems

Among the goals of designing 'Trojan-Horse' like NP drug-delivery systems was to achieve the loading of multiple chemotherapeutic agents in tandem in a controllable and quantifiable manner to allow for their enhanced tumour targeting and to reduce overall dosages of drugs required for cancer treatment. Seeking to apply the concept of small molecule EGFR inhibitor synergism with

DNA-damaging agents in clinical practice using nanocarriers, Morton et al. (2014) developed folate-functional liposomes capable of a 'shell first, core second fashion' drug release. Here, the lipid envelope was used for storage of Erl, and the aqueous interior was used to house Dox during NP administration and accumulation, as seen in Figure 2. Researchers were able to demonstrate the sequential release of Erl followed by core unloading of Dox, resulting in an increase in treatment cytotoxicity as measured *in vitro* and *in vivo*. This particular design of liposome, however, could not control the sequenced release of drugs precisely. As well, a challenge inherent to the use of liposomes as a tumour targeting system is that, despite extensive surface 'decoration', shown in Figure 3, their success is still in part dictated by protein heterogeneity and the numbers of biomarkers on the cancer cell surfaces (Zhao et al., 2013).

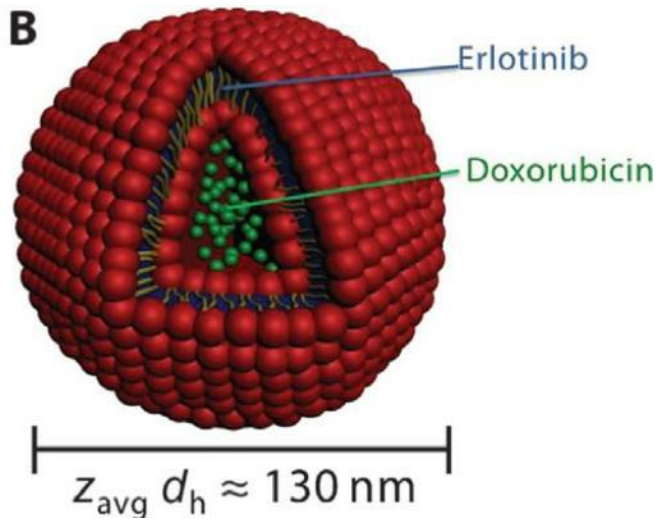

Figure 2: Schematic of dual loading of a small-molecule inhibitor (erlotinib, blue) into the hydrophobic, vesicular wall compartment and of a cytotoxic agent (doxorubicin, green) into the aqueous, hydrophilic interior (Morton et al., 2014).

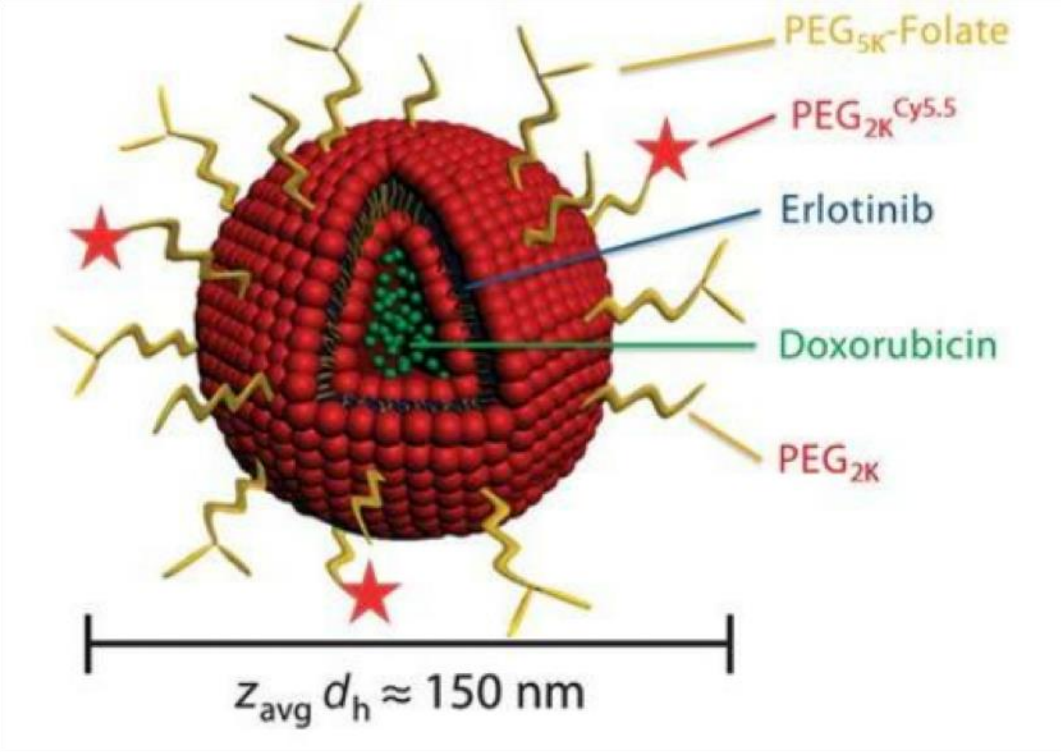

Figure 3: Schematic of addition of DSPE-PEG2K (0.5 mol% ratio) to minimize nonspecific protein binding, DSPE-PEG2KCy5.5 (0.1 mol% ratio) for fluorescent tracking, and DSPE-PEG5K-folate (0.5 mol% ratio) for cell-targeted delivery (Morton et al., 2014).

Compared to active targeting ligand decoration used in liposomal NP cancer-drug delivery, nanosystems using the lower pH of the tumour microenvironment to enhance cancer cell internalization can be more specific for drug delivery, avoid off-target effects, and can be exploited for the treatment of any tumour (Lee, Gao and Bae, 2008; Ge and Liu, 2013; He et al., 2016; Riaz et al., 2018). To this end, He et al. (2016) used a pH-sensitive lipid bilayer (HHG_2C_{18}-L) to coat amino-functionalized mesoporous silica NPs (MSN-NH_2) loaded with both Erl and Dox (M-HHG_2C_{18}-L(E + D)) to test drug delivery against lung cancer models *in vitro* and *in vivo*, the design of which is illustrated in Figure 4. In these NPs, HHG_2C_{18}-L contained 1,5-dioctadecyl-L-glutamyl 2-histidyl-hexahydrobenzoic acid (HHG_2C_{18}), which displayed a negative charge at physiological pH and reversed from negative to positive when exposed to the

acidic tumour microenvironment (Mo et al., 2013; He et al., 2016). Upon entering cancer cells, Erl was sequestered in the exterior of the lipid bilayer for release (He et al., 2016). Within the cells, HHG_2C_{18}-L would become even more positively charged, inducing a coulombic repulsion with MSN-NH_2, leading to destabilization and the sequential release of Dox. Despite the enhanced synergistic effect between Dox and Erl on cancer cell cytotoxicity demonstrated through this method of NP drug-delivery, the quantification of accumulating *in vitro* drug concentrations revealed the time lag between the release of these two agents was relatively imprecise. Specifically, while Erl release was observed immediately following NP administration, Dox was recorded to accumulate between 20-30 minutes post administration. This has led other researchers to believe that both endogenous and exogenous stimuli should be considered together to better control the order and delay between multi-drug release in tumours (Feng et al., 2019).

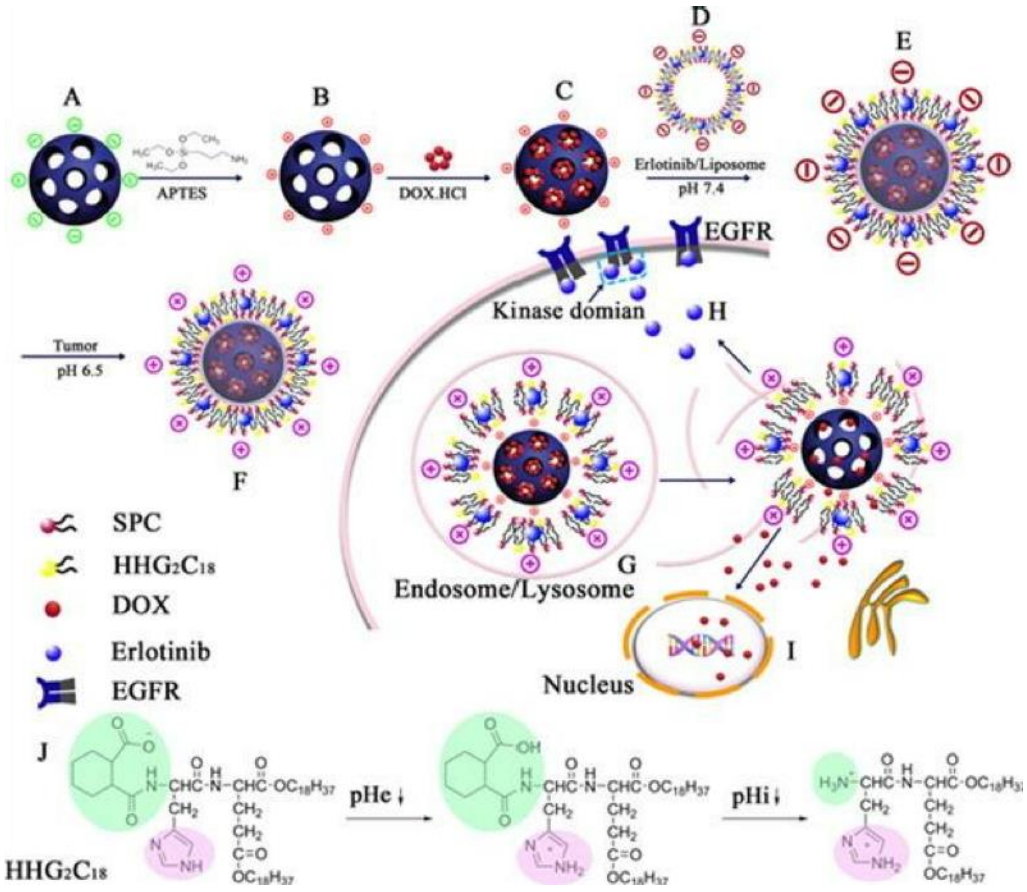

Figure 4: Schematic illustration of preparation of erlotinib/Dox combination co-delivery nanocarriers and synergistic therapy of erlotinib and Dox. The surface of mesoporous silica nanoparticles (A) were modified with 3-aminopropyltriethoxysilane (APTES) to form MSN-NH_2 (B). MSN-NH_2 were then loaded with Dox to obtain Dox-loaded MSN-NH_2 (C), followed by support with erlotinib-loaded lipid bilayer (D) to yield M-HHG_2C_{18}-L(E + D) (E). After injection of M-HHG_2C_{18}-L(E + D), the nanoparticles accumulated at the tumor site through the EPR effect in tumor blood vessels. M-HHG_2C_{18}-L(E + D) were positively charged in the extracellular environment (F) leading to easy internalization by tumor cells. After cell uptake, as erlotinib was loaded in the exterior lipid bilayer and the controlled release ability of MSN-NH_2, erlotinib released faster than Dox. Additionally, the lipid bilayer was more positive and induced a strong repulsion with MSN-NH_2 in intracellular environment (G), enhancing sequential staggered release of erlotinib and Dox, which was pretreated and staggered to inhibit kinase domain of EGFR in cell membrane (H) and was targeted to cell nucleus (I) respectively, thus maximized the synergistic therapy. Effect of extracellular and intracellular pH (pH_e and pH_i), respectively on the HHG_2C_{18} (J) (He et al., 2016).

1.5 *In Vitro* Assessments of Chemotherapeutic Agents and Nanoparticles

1.5.1 2D Cell Viability and Cytotoxicity Assays

Cell viability and cytotoxicity assays are widely used to test chemicals and approved or potential drugs against various cell types, particularly in oncological research since they allow an assessment of compound toxicity and tumor cell growth inhibition (Aslantürk, 2018). These assays also serve as a means of analyzing NP cytotoxicity (Stone, Johnston, and Schins, 2009), and comparing the therapeutic efficacy of free and NP-based drug delivery (Patra et al., 2018; Jain and Thareja, 2019). Cell viability and cytotoxicity assays can be based on a variety of cell functions such as enzyme activity, cell adherence, ATP production, co-enzyme production, nucleotide uptake activity, organelle function, and cell membrane permeability (Ishiyama et al., 1996; Aslantürk, 2018). More generally, however, such assays can be divided into those that assess either metabolic functionality or membrane viability (live/dead assays).

Cell viability and cytotoxicity assays focused on metabolic functionality, such as the 3-(4,5-dimethylthiazol-2-yl)-2,5-diphenyltetrazolium bromide (MTT) assay, are commonly used to examine drug and chemical toxicity, though each has innate advantages and disadvantages based on the specific mechanisms on which they rely (Angius and Floris, 2015; Aslantürk, 2018). One common disadvantage amongst these assays is that molecular uptake – and by extension efficacy and toxicity – often occurs based on interactions with receptors and is therefore dependent on receptor expression and chemical specificity and selectivity (Kell and Oliver, 2014; Salatin and Khosroushahi, 2017). As well, in terms of NP-based drug delivery, metabolism-based assays used to determine NP toxicity *in vitro* may experience interference due to sub-lethal cellular changes that can alter certain functions of the cell but do not result in cell death (Kong et al.,

2011). Despite the limitations of *in vitro* viability assays that rely on cellular metabolic pathways, they remain important in interpreting the effects of chemicals and NPs on cellular pathways and overall cellular viability.

Many cell assays are also used specifically to perform live versus dead cell counts, a simple example being Tryptophan blue exclusion, as a means of assessing cellular toxicity (Stone, Johnston, and Schins, 2009). The premise for assays such as this is that cells with an intact membrane are able to resist uptake of an indicator and therefore appear normal upon examination using light microscopy. Dead cells, on the other hand, are unable to maintain an intact plasma membrane and would appear stained after exposure. While dye exclusion itself may be a rapid measure of cell viability or toxicity, it is subject to error since viability is being determined indirectly from cell membrane integrity and thus may incur false positives or negatives (Strober, 2015). It should be noted that other means of employing dye exclusion exist, such as the use of flow cytometry, though this method also faces its own challenges with accuracy (Strober, 2015; Aslantürk, 2018). As with assays that rely on metabolic pathway assessment, membrane viability assays cannot themselves completely reveal a chemical's toxicity. A combination of these two categories of assays, however, may provide a much more thorough understanding of both free chemical, and bare and drug-loaded NP-based toxicity.

1.5.2 3D Cell Spheroid Assays

Over time there has been a distinct decline in the discovery of novel medications, which has put pressure on researchers to re-evaluate the efficacy and even validity of the modern drug discovery process (Allison, 2012; Scannell, et al., 2012; Horvath et al., 2016). A proposed cause

for this failure is the reliance on 'reductionist' biological models involving the use of immortalized cell lines cultured in an unnatural 2D setting for preclinical drug trials. It is increasingly well understood that cell monolayers have little in common with the complex 3D multicellular structures and organization found in living organisms (Horvath et al., 2016). As a result, many researchers have sought to develop more appropriate cell models that better represent human and disease physiology for drug screening. One such example is the multicellular cell spheroid model (Hirschhaeuser et al., 2010; Weiswald, Bellet and Dangles-Marie, 2015). This model is particularly favoured because it is relatively easily standardized yet provides enough complexity to represent certain aspects of human healthy and diseased tissues such as 3D geometry, physical, chemical, and biological gradients, cell stratification, and functional differentiation (Hirschhaeuser et al., 2010; Nath and Devi, 2016; Thoma et al., 2014). There also exist a number of techniques that can be used for generating spheroids, such as the use of hanging drops (Kelm et al., 2003) or levitation (Haisler et al., 2013).

The principal behind the use of the spheroid model for drug screening is that the 3D structure will allow for more efficient identification of anti-cancer therapeutics and demonstrate more accurately the risk of such drugs to normal cells (Mittler et al., 2017). As such, spheroids have become widely used as a means of testing cytotoxicity. Due to their larger size, spheroid assays allow for cytotoxicity to be followed over time by measuring the size and shape of spheroids (Vinci et al., 2012; Baek et al., 2016; Zanoni et al., 2016). As well, complex processes like tumour penetration and angiogenesis can be modeled with cancer cell spheroids, and the effects of chemotherapeutic drugs can be studied in this context with simple bright-field microscopy (Vinci et al., 2012; Vinci, Box, and Eccles, 2015). The effects of drugs on cell composition,

localization, and functional status within the spheroids can also be analyzed using different means of fluorescent observation (Weiswald et al., 2010; Dufau et al., 2012; Smyrek and Stelzer, 2017).

Spheroid assays can also be used to specifically examine the toxicity of bare and drug-carrying NPs to healthy and diseased tissues (Lee et al., 2009; De Simone et al., 2018; Tchoryk et al., 2019). As the use of spheroid assays has become more common, it has been revealed that they provide relevant insight into NP and drug delivering NP toxicity and therapeutic efficacy, particularly for cancer treatment (De Simone et al., 2018; Tchoryk et al., 2019). Such studies have even shown that in some cases NP toxic effects are significantly reduced in healthy cell spheroid culture when compared to the equivalent 2D cultures (Lee et al., 2009). In light of these benefits, it is crucial moving forward to assess previously implemented and newly designed NP drug-delivery systems using 3D cell assays and cancer models in order to identify and progressively overcome the challenges they will face under physiological conditions, thereby improving their viability and efficacy during clinical application.

PART 2: REPORT

2.1 Introduction

2.1.1 Cancer Incidence, Mortality, and Treatment

Cancer is currently the leading cause of death in Canada (Statistics Canada, 2020), and the second leading cause of death worldwide (World Health Organization, 2018). Over the past several years, the number of new cancer diagnoses as well as cancer-related deaths has increased annually both nationally and internationally, and this trend is expected to persist. Modern medicine is capable of a number of antitumour therapeutic approaches, including surgery, chemotherapy, radiotherapy, hormone therapy, and immunotherapy (Bahrami et al., 2017), though each treatment option faces its own unique challenges that hindered its clinical benefit (Perez et al., 2008; Ross et al., 2000; Keereweer et al., 2013; Schaue and McBride, 2015; Sambi, Bagheri and Szewczuk, 2019). With such persistently high incidence and mortality rates, it is critical that new and more effective means of combating this disease be developed. One mode of diagnosis, imaging, and most critically chemotherapeutic drug delivery currently under intensive investigation is the use of nanoparticles (NPs). In the context of cancer treatment, NPs are capable of delivering chemotherapeutic drugs directly to tumours and within cancer cells, and have been shown to enhance treatment efficacy while reducing the severity of side effects commonly observed with traditional ‘free’ small-molecule chemotherapeutics (Davis, Chen, and Shin, 2008; L. Li et al., 2015; Y. Li et al., 2015).

2.1.2 Nanoparticle-based Drug Delivery Research

NP drug delivery systems have been extensively researched since 1986 when the enhanced permeability and retention (EPR) effect was first described (Matsumura and Maeda, 1986;

Egusquiaguirre et al., 2012). Using mouse models, researchers observed that macromolecules and NPs accumulated in tumour tissue more readily than in normal tissue, supposedly due to leaky vasculature present within tumours. This finding ultimately led to the emergence of nanomedicine, described as the application of nanotechnology to medicine and healthcare (Matsumura and Maeda, 1986; Wagner et al., 2006). Despite the EPR effect serving as the rationale for many drug nanocarrier designs – the development of which have cost billions of dollars over several decades – data suggests that this phenomenon only marginally improves experimental NP-based drug delivery (Nichols and Bae, 2014; Danhier, 2016). In spite of this, there are currently a number of nanoparticle therapeutics as well as imaging agents and technologies that have been approved for clinical use largely based on their advantages over non-formulated and free drug administration, such as their ability to deliver therapeutics and treat areas of the body that other delivery systems cannot reach, to reduce systemic toxicity of the drugs administered, and to reduce the overall dosage necessary for achieving therapeutic drug concentrations in a target area (Anselmo and Mitragotri, 2016).

Further investigation into the means through which NPs can accumulate in tumours has revealed an alternative mechanism involving the use of a metabolically active transport process across endothelial cells – transcytosis – is likely responsible for this phenomenon (Sindhwani et al., 2020). In fact, with NPs of certain sizes, this active means of transport can account for 75-97% of total NP accumulation in tumours. While active transport may be the primary means of NP accumulation based on this research, it is important for current and future nanocarrier designs and applications in cancer treatment that the specific mechanisms of systemic circulation, tumour

accumulation, and tumour penetration be investigated for each drug delivery system to develop their clinical efficacy.

2.1.3 Barriers to Nanoparticle-based Drug Delivery

To serve as an effective method of cancer drug delivery, NPs must overcome several physiological barriers that impose conflicting requirements on both their size and charge. These barriers limit a NP's ability to remain in the blood during circulation after intravenous (IV) administration, accumulate at the site of action, and penetrate a tumour to deliver a chemotherapeutic agent (B. Chen et al., 2017).

In order for NPs to remain in the bloodstream and avoid rapid renal excretion, aggregating with plasma proteins and being eliminated via the reticuloendothelial system or off-target cell interactions, their surface must be negatively charged or neutral (Ma et al., 2005; Hatakeyama et al., 2006; L. Li et al., 2015; B. Chen et al., 2017). The kidney's filtration system – glomeruli containing three layers with varying pore sizes – also imposes an effective NP minimum size cutoff for their overall structure of 10 nanometres (nm) (Soo Choi et al., 2007). As well, NPs with a diameter greater than 200 nm activate the body's complement filtration system, causing their removal from the bloodstream and accumulation in the liver and spleen (Faraji and Wipf, 2009; de Barros et al., 2012; Nesargikar, Spiller, and Chavez, 2012; Kulkarni and Feng, 2013). While 10 and 200 nm represent the absolute size boundaries for NPs capable of circulating throughout the body without being at risk of filtration or removal, studies suggest that a maximum size limit of 100-150 nm for most NPs allows them to circulate longer while concurrently avoiding elimination (Moghimi, Hunter, and Andresen, 2012; Hoshyar, Gray, Han and Bao, 2016).

Another challenge with the use of chemotherapeutic carrying NPs is ensuring their accumulation at the site of a tumour. Studies have shown that NPs of around 100 nm accumulate well at tumours – either due to the EPR effect (Matsumura and Maeda, 1986; O'Brien et al., 2004; Cabral et al., 2011; Jinqiang Wang et al., 2015) or more likely due to active transendothelial transport (Sindhwani et al., 2020) – at therapeutic concentrations. Once NPs have accumulated at the site of a tumour, they must then penetrate it in order to effectively deliver their chemotherapeutic drug; however, the size of the NP that best allows for tumour penetration is much smaller than that for accumulation. Tumor core penetration, and by extension high therapeutic efficacy, is achieved by NPs of 30 nm or less due to the extremely small interstitial space between tumour cells (Cabral et al., 2011; Jie Wang et al., 2015), or 100 nm or less based on trans-endothelial transport mechanisms (Sindhwani et al., 2020). Furthermore, while possessing a negative charge or remaining neutral supports their circulation in the bloodstream and minimizes off-target effects, positively charged NPs have superior electrostatic interactions with negatively charged tumour cell membranes, leading to improved cellular uptake (Ma et al., 2005; Hatakeyama et al., 2006; L. Li et al., 2015; B. Chen et al., 2017).

2.1.4 Multi-drug Cancer Therapy

In order to enhance the efficacy of chemotherapy-based cancer treatment, researchers have examined the effects that administering multiple drugs in succession or simultaneously have on the therapeutic potential of chemotherapy and drug delivery systems (Lee et al., 2012; Morton et al., 2014). While seeking to identify new strategies for enhancing the initial chemosensitivity of triple-negative breast cancers, Lee et al. (2012) explored whether manipulating the interface between growth factor and DNA damage signaling pathways in tumor cells could modulate the therapeutic response of this tumor type. Researchers were ultimately able to determine that

pretreatment with epidermal growth factor receptor (EGFR) inhibitors, such as the hydrophobic drug erlotinib (Erl), can synergize with the apoptotic response of cancer cells to DNA-damaging chemotherapy, such as with the hydrophilic drug doxorubicin (Dox). This observed synergy is believed to have occurred through a 'rewiring' of oncogenic signaling networks and 'unmasking' of apoptotic pathways involving caspase-8, a member of the cysteine proteases that are implicated in apoptosis and cytokine processing (Barnhart, Alappat and Peter, 2003; Lee et al., 2012; Morton et al., 2014). It should be noted that while these findings indicate the possibility of increasing the efficacy of chemotherapeutic drugs, synergism between the EGFR inhibitors and DNA-damaging agents was observed to be both dose and schedule-dependent (Lee et al., 2012). Specifically, it has been found that when Erl is administered at least 4 hours prior to Dox, synergism can be observed *in vitro* (Lee et al., 2012). However, in order to maximize the synergistic effects of this combination chemotherapy, it has been found that there needs to be a specific time lag of 24 hours between the administration of each drug. Further, the enhanced sensitivity of cancer cells to Dox was observed to require sustained inhibition of EGFR, since it was the activity of the EGFR pathway rather than simply EGFR expression that determined whether time-staggered inhibition resulted in a synergistic cytotoxic effect.

2.1.5 Starch Nanoparticle Clusters

Previous work in our lab has demonstrated the ability to fabricate starch NP (SNP)-based electrostatic complexes, or nanoclusters, of 100-160 nm in size that are composed of slightly cationic SNPs (~20 nm diameter) bound to anionic poly(oligoethylene glycol methacrylate) (POEGMA) functionalized with 2,3-dimethylmaleic anhydride (POEGMA-Hyd-DMA), which possesses charge-switchable properties. The method through which these nanoclusters are

formed also allows for the manipulation of the material mass ratio combinations, providing opportunity for the customization of nanoclusters to achieve appropriate sizes for circulation in the bloodstream, and effective SNP-bound chemotherapeutic drug concentrations for therapeutic efficacy.

2.1.6 Nanocluster Circulation, Disassembly, and Starch Nanoparticle Release

Nanoclusters possess therapeutic efficacy *in vitro* and *in vivo* based on their ability to remain stable at physiological pH (7.4) and disassemble to release the highly penetrable SNPs when exposed to the acidic microenvironment associated with tumours. The initial size of these clusters ensures they are able to circulate through the bloodstream upon IV administration without being removed by the kidney's filtration system or being targeted for removal by the complement filtration system (Soo Choi et al., 2007; Faraji and Wipf, 2009; Kulkarni and Feng, 2013). Their size range also meets most recommendations for maximum size limits of NPs that allow them to circulate longer and avoid elimination (Moghimi, Hunter, and Andresen, 2012; Hoshyar, Gray, Han and Bao, 2016). The polymer used in these nanoclusters possesses a hydrazide group conjugated with DMA via an amide bond. The DMA contains an outer carboxylic acid group which, under physiological pH conditions at which the amide is relatively stable, imparts a negative charge (Ooi et al., 2020). Given that the polymer is the dominant material, the nanoclusters as a whole then possess a negative charge, which allows them to avoid rapid renal excretion, aggregating with plasma proteins and being eliminated via the reticuloendothelial system and off-target cell interactions (Ma et al., 2005; Hatakeyama et al., 2006; L. Li et al., 2015; B. Chen et al., 2017).

Upon accumulation at the site of a tumour, likely by active transendothelial transport, these nanoclusters undergo a low pH-stimulated disassembly. The extracellular environment of most tumours is acidic compared to normal tissues, with a pH range of 6.5-7.2 (Cardone, Casavola and Reshkin, 2005; W. Chen et al., 2017; Zhou et al., 2018). As well, a low pH range of 4.5-5.5 also exists in organelles such as endosomes and lysosomes (Liu et al., 2014). At these lower pH ranges, the cleavage of the amide bond linking the DMA group to the polymer backbone becomes significantly more hydrolytically labile and the DMA group is released, exposing the buried hydrazide group. This results in the polymers developing a more neutral charge, which causes a loss of electrostatic interactions with the embedded cationic SNPs and ultimately disassembly. This disassembly step then releases the SNPs that possess the appropriate size to subsequently penetrate tumour cores (Cabral et al., 2011; Wang et al., 2015). The use of these nanoclusters in this case enhances the ability of the drug loaded onto the SNPs to be delivered intratumourally as opposed to only the surface of the tumour, raising the overall cytotoxic impact.

2.1.7 Starch Nanoparticle Versatility

Cationic SNPs are extremely versatile with an ideal size for tumour penetration and an ability to be functionalized with various functional groups that allow for direct interactions with different chemotherapeutic drugs. In addition, depending on their functionalization, cationic SNPs can be made to possess different magnitudes of charge, either directing them more towards tumour core penetration (‘penetrable’ less cationic SNPs) or cancer cell uptake (‘sticky’ more cationic SNPs).

2.1.8 Multi-drug Loaded Starch Nanoparticle Clusters

The objective of this research was to generate SNP clusters loaded with both hydrophilic and hydrophobic drugs in tandem. The procedure to develop these dual drug-loaded SNP clusters involved exploiting the versatility of SNPs to generate hydrophilic and hydrophobic SNP variants capable of loading the hydrophilic drug Dox and the hydrophobic drug Erl respectively, which have been chosen based on their previously reported cytotoxic synergism against cancer cells. These SNP variants could then be used to generate dual SNP carrying nanoclusters with different ratios of Dox- and Erl-loaded SNPs to examine their synergistic effect using 2D and 3D cell assays *in vitro*, and eventually *in vivo* using a transgenic mouse model.

2.2 Materials and Methods

2.2.1 Materials

Experimental grade cationic SNPs (waxy starch with 100% amylopectin and a fully amorphous internal structure, lot number unavailable[1]) were provided by EcoSynthetix Inc. (Burlington, ON). Sodium periodate ($NaIO_4$), (≥99.8%), 4-bromobenzaldehyde (99%)**,** oligoethylene glycol methacrylate ($OEGMA_{475}$), acrylic acid (AA, 99%), thioglycolic acid (TGA, 98%), 2,3-dimethylmaleic anhydride (DMA, 98%), N,N-dimethylformamide (DMF, 99.8%, anhydrous), 2-octen-1-ylsuccinic anhydride (OctSAn, mixture of cis and trans, 97%), and sodium bicarbonate ($NaHCO_3$, ≥99.7%) were all received from Sigma Aldrich (Oakville, ON). 2,2-azobisisobutryic acid dimethyl ester (AIBMe, 98.5%) was received from Wako Chemicals. Adipic dihydrazide (ADH, 97%) was received from Alfa Aesar, and 1-(3-dimethylaminopropyl)-carbodiimide hydrochloride (EDC, commercial grade, 99%) was received from AK Scientific. All chemicals

[1] Lot number available on the cationic SNP (EcoSynthetix Inc.) container stored in the Hoare Lab.

were used as received. For all experiments, Millipore Milli-Q grade distilled deionized water (MQW, 18.2 MΩ cm resistivity) was used.

2.2.2 Synthesis of Aldehyde-functionalized Starch Nanoparticles

Two different methods of synthesizing aldehyde-functionalized SNPs (Ald-SNPs) were examined in this work, one using $NaIO_4$, and the other using 4-bromobenzaldehyde. The latter of these two methods was added to accommodate for a drawback of the $NaIO_4$-functionalization based SNPs revealed during later testing, which is discussed in section 2.3.1.

2.2.2.1 Sodium Periodate-based Aldehyde Functionalization of Starch Nanoparticles

For the $NaIO_4$-based Ald-SNP synthesis, a 30 g aqueous dispersion of cationic SNPs (12.5% w/v in MQW) was reacted with a 55 mL solution of $NaIO_4$ (dissolved at a mass of between 1.820 g to 9.102 g depending on the desired degree of substitution between 0.10-0.50 of anhydrous glucose units). Both solutions were added to a 250 mL round-bottomed flask that was darkened with tinfoil to minimize radical formation. The flask was placed under magnetic stirring for 4 hours, at which point an equimolar amount of ethylene glycol was added to quench any remaining periodate ions. The sample remained under magnetic stirring overnight (15-24 hours), at which point the Ald-SNPs were dialyzed against MQW for three days – during which time the water was changed six times, once every 12 hours (6 x 12 dialysis cycles) – using a 3.5 kDa molecular weight cut-off membrane. The sample was then lyophilized to dryness and stored in the dark. Ald-SNPs from this synthesis were then characterized by ^{1}H NMR spectroscopy (data unavailable[2]).

[2] Analysis incomplete at this time.

2.2.2.2 4-bromobenzaldehyde-based Aldehyde Functionalization of Starch Nanoparticles

For the 4-bromobenzaldehyde-based Ald-SNP synthesis, the pH of a 20 g aqueous dispersion of cationic SNPs (10% w/v in MQW) inside a 250 mL round-bottomed flask was raised to 9.0 or above with the addition of 1 M sodium hydroxide (NaOH) as required. 8 g of 4-bromobenzaldehyde was dissolved in 40 mL of DMF and subsequently added to the SNP solution. The flask was immediately partially submerged in an oil bath set to 70 °C with the solution under magnetic stirring for 24 hours. The pH of the solution was monitored for a minimum of 4 hours using pH test paper and kept above 9.0 with the addition of 1 M NaOH as required. The solution was then allowed to cool and underwent air purging for 12 hours or until completely dry to remove DMF. The Ald-SNPs were then re-dissolved in 150 mL of MQW and dialyzed against MQW over 6 x 12 dialysis cycles using a 3.5 kDa molecular weight cut-off membrane. The sample was then filtered to remove any SNP aggregates, dialyzed for two more 12-hour cycles to ensure trace DMF was removed, and lyophilized to dryness for storage.

2.2.3 Synthesis of Octenyl Succinic Anhydride-functionalized Starch Nanoparticles

To begin generating the OctSAn-functionalized SNPs (OctSAn-SNPs), a 100 g aqueous dispersion of cationic SNPs (5% w/v in MQW) inside a 250 mL round-bottomed flask was mixed with 0.074 g of $NaHCO_3$ and placed under magnetic stirring. The pH of the solution was monitored for 1 hour using a pH probe and kept between 10 and 11 (10.4 was ideal) by adding 1.0 M NaOH as required. 0.649 g of OctSAn was then added dropwise over the course of 1 hour while a pH of 10-11 was maintained. The pH was then monitored for an additional 30 minutes before the sample was neutralized to pH 7 with the addition of 1.0 M hydrochloric acid (HCl).

The OctSAn-SNPs were then dialyzed against MQW over 6 x 12 dialysis cycles using a 3.5 kDa molecular weight cut-off membrane and lyophilized to dryness for storage.

2.2.4 Synthesis and Characterization of POEGMA-Hyd-DMA Polymers

Unfunctionalized polyOEGMA (POEGMA)-AA was prepared by first adding 115 mg of AIBMe, 1.517 g of AA, 10.00 g of $OEGMA_{475}$, and 30-40 μL (depending on the desired degree of polymerization) of TGA (previously diluted to 10% in 1,4-dioxane) to a 250 mL round-bottomed flask in sequence. 40 mL of 1,4-dioxane was then added to the flask, and the solution was purged with nitrogen for 40 minutes at room temperature. The flask was then sealed and submerged in a preheated oil bath at 75 °C for 4 hours under magnetic stirring. After polymerization, the solvent (1,4-dioxane) was removed by rotary evaporation and the remaining POEGMA-AA was dialyzed against MQW over 6 x 12 dialysis cycles using a 3.5 kDa molecular weight cut-off membrane, and subsequently lyophilized to dryness. The polymer was then dissolved in MQW at 10% w/v and stored at 4 °C. The number-average molecular weight (M_n) of the POEGMA-AA was determined using gel permeation chromatography (GPC), and the degree of carboxylic acid functionalization was assessed by conductometric base-into-acid titration (data and subsequent calculations can be found in Supplementary Files 1 and 2 respectively). POEGMA-Hyd was prepared following the dissolution of the POEGMA-AA copolymer by adding 18.3 g of ADH (corresponding to 5 times the moles of AA added) to the flask, at which time the pH was adjusted to 4.75 using 1.0 M HCl, as well as 8.17 g of EDC (corresponding to 2 times the moles of AA added), after which the pH was maintained at 4.75 by the dropwise addition of 1.0 M HCl over 4 hours as required. The solution was left to stir overnight, dialyzed against MQW over 6 x 12 dialysis cycles using a 3.5 molecular weight cut-

off membrane and lyophilized to dryness. The polymer was again redissolved in MQW water at 10% w/v and stored at 4 °C. The M_n of the POEGMA-Hyd was determined using GPC (data unavailable[3]). The degree of hydrazide functionalization was assessed using conductometric base-into-acid titration comparing the carboxylic acid content before and after ADH conjugation (0.1 M NaOH titrant, 50 mg polymer in 50 mL of 3 mM sodium chloride (NaCl) solution, ManTech automatic titrator) (data and subsequent calculations can be found in Supplementary Files 1 and 2 respectively). POEGMA-Hyd-DMA was prepared by first adding 4.84 g of DMA to the POEGMA-Hyd at 10% w/v (0.55 g of DMA per gram of dried POEGMA-Hyd) under magnetic stirring. The pH of the solution was raised to 9.0 with the addition of 1.0 M of NaOH as required. The pH was then monitored using litmus paper for 4 hours, and the reaction was allowed to run for a total of 24 hours. The sample was then dialyzed against MQW over 6 x 12 dialysis cycles using a 3.5 kDa molecular weight cut-off membrane and lyophilized to dryness. Additional characterizations involving ^{1}H-NMR and size exclusion chromatography were also conducted for the POEGMA polymers (see Supplementary File 3).

2.2.5 Size Measurements of Starch Nanoparticles

The sizes of SNPs were determined using a Brookhaven 90Plus particle size and zeta potential analyzer with dynamic light scattering (DLS). For each sample, DLS measurements were run using a light beam of 659 nm and had particle sizes read at 37 °C for 60 seconds six times with 1 second intervals between readings and an initial equilibration time of 120 seconds. Prior to DLS analysis, SNP solutions of 100 mg/mL in MQW were prepared (2-4 mL per sample), vortexed for 20 seconds, and subsequently placed in an incubator for 24 hours at room temperature.

[3] Data collected and stored in the Hoare Lab.

Samples were then centrifuged at 10,000 rotations per minute (RPM) for 10 minutes at 20 °C. The supernatants were transferred to 20 mL glass wells, and the pellets (consisting of SNP aggregates) were discarded. 0.5 mL of the sample SNP supernatants were then added to 10 mm cuvettes along with 1.5 mL of MQW and underwent mixing by inversion 5 times before being measured. SNP measurements were examined using the 'log' and 'number' outputs where graphical peaks represented the number of readings of a particular particle size, which were normalized to the most common reading. The number average for each peak was used when interpreting the data.

2.2.6 Zeta Potential Measurements of Starch Nanoparticles

The zeta potentials of each SNP sample were determined using a Brookhaven 90Plus particle size and zeta potential analyzer. Each sample had its zeta potential measured six times at 37 ℃ for 30 cycles with a 1 second interval between readings and an initial 180 second equilibration time. Prior to zeta potential readings, SNP solutions of 100mg/mL in MQW were prepared and vortexed for 20 seconds (2-4 mL per sample), and subsequently placed in an incubator for 24 hours at room temperature. Samples were then centrifuged at 10,000 RPM for 10 minutes at 20 °C. The supernatants were transferred to 20 mL glass wells, and the pellets (consisting of SNP aggregates) were discarded. 0.5 mL of the sample SNP supernatants were then added to 10 mm cuvettes along with 1.5 mL of a 5 mM sodium chloride (NaCl) solution and underwent mixing by inversion 5 times before being measured. Zeta potential outputs were analyzed using the Smoluchowski zeta potential model.

2.2.7 Zeta Potential Measurements of POEGMA-Hyd-DMA Polymers

The zeta potentials of POEGMA-Hyd-DMA were determined using the same technical specifications as were used for SNP readings. Prior to zeta potential readings, POEGMA-Hyd-DMA samples were dissolved at 10% w/v. 0.5 mL of the polymer sample supernatants were then added to 10 mm cuvettes along with 1.5 mL of a 5 mM NaCl solution and underwent mixing by inversion 5 times before being measured. Zeta potential outputs were again analyzed using the Smoluchowski zeta potential model.

2.2.8 Doxorubicin Loading onto Aldehyde-functionalized Starch Nanoparticles

To prepare Dox loaded SNPs (Dox-Ald-SNPs), Ald-SNPs were dissolved at 10 weight percentage (10 wt%) in MQW and Dox was dissolved at a concentration of 10 mg/mL in dimethyl sulfoxide (DMSO). The Ald-SNP and Dox solutions were mixed at a mass ratio of 10:1 Ald-SNP:Dox, and left to stir for 24 hours in the absence of light. The solution was then dialyzed against MQW over 6 x 12 dialysis cycles using a 3.5-5 kDa molecular weight cut-off membrane, after which time the sample was lyophilized to dryness for storage.

2.2.9 Generating Single Starch Nanoparticle Carrying Nanoclusters

To start, SNPs and POEGMA-Hyd-DMA were dissolved separately in 15 mL Falcon tubes with MQW and 1.0 M NaOH respectively to generate material concentrations of 100 mg/mL. Samples were then centrifuged at 10,000 RPM for 10 minutes at 20 °C, after which the supernatants were transferred to 20 mL glass wells and the pellets (consisting of SNP and polymer aggregates respectively) were discarded. In these nanoclusters, a 10:90 mass ratio of SNPs to POEGMA-Hyd-DMA was used. Here, 0.9 mL and 8.1 mL of the SNP and POEGMA-

Hyd-DMA supernatants respectively were added to a 20 mL glass sample jar. All samples were subsequently kept under high magnetic stirring for 24 hours before storage at 4 °C.

2.2.10 Quantification of Doxorubicin Loading in Aldehyde-functionalized Starch Nanoparticle Carrying Nanoclusters

In order to quantify the loading efficiency of Dox into Ald-SNP containing nanoclusters, solid Dox-Ald-SNPs were used in the nanocluster synthesis method described in 2.2.8. Dox concentration was then measured using fluorescence intensity (emission signal at 595 nm upon excitation with a 470 nm laser) and determined using a standard curve.

2.3 Results and Discussion

2.3.1 Starch Nanoparticle Characterization

To characterize the three types of SNPs synthesized, the first analyses conducted were of the sizes and zeta potentials of SNPs in pure samples, shown in Figure 5. In the case of the $NaIO_4$-based Ald-SNPs, DLS revealed a single peak with an average of approximately 19 nm using a number distribution (Figure 5A), representing the predominant particle diameter. The mean zeta potential for the 6 measurements of these SNPs was determined to be approximately 12 millivolts (mV), as seen in Table 1, These findings indicate that the $NaIO_4$-based Ald-SNPs possess the appropriate size and charge for interactions with, and loading of, the hydrophilic drug Dox and use as an ionic building block to form SNP-based nanoclusters.

In the case of the OctSAn-SNPs, a single peak was observed with an average of approximately 22 nm using a number distribution (Figure 5B), again representing predominant particle

diameter. The mean zeta potential for the 6 measurements of these SNPs was determined to be approximately 5 mV, as seen in Table 1. Given the similarity in size and size distribution of the OctSAn-SNPs to the $NaIO_4$-based Ald-SNPs (Figure 5C), it is likely that they are suitable for use in generating SNP-based nanoclusters. The low positive zeta potential also suggests that these OctSAn-SNPs are 'hydrophobized' compared to the $NaIO_4$-based Ald-SNPs, possessing a nearly neutral but still cationic charge, which may both benefit and hinder the use of these SNPs in therapeutic nanoclusters. The lower cationic charge of the OctSAn-SNPs is likely to allow for their interaction with and loading of the hydrophobic drug Erl; however it may also lower the loading efficiency of these SNPs into nanoclusters due to weakened electrostatic interactions with the negatively charged polymers, thereby reducing overall nanocluster loading efficiency of Erl. To examine this further, OctSAn-SNP-based nanoclusters and dual-SNP loaded nanoclusters must be examined under both physiological and acidic conditions to assess SNP loading, disassembly and SNP release.

Repeated DLS analyses revealed that the $NaIO_4$-based Ald-SNPs undergo unexpected degradation in storage over a relatively short time period (data unavailable[4]). This motivated the design of a second method of synthesizing Ald-SNPs using 4-bromobenzaldehyde as described in 2.2.2.2. DLS of the 4-bromobenzaldehyde-based Ald-SNPs revealed two peaks, one with an average of approximately 230 nm and another with an average of approximately 3,500 nm using a number distribution (Figure 5D). Based on the size and variability of DLS readings, it is believed that this particular Ald-SNP sample underwent functional degradation and structural aggregation due to prolonged storage in and exposure to DMF after the sample was allowed to

[4] Data collected and stored in the Hoare lab.

cool to room temperature prior to drying. A zeta potential analysis of this sample was not conducted, and resynthesis is necessary before it can be determined if SNPs 4-bromobenzaldehyde-based Ald-SNPs are suitable for loading Dox and use in SNP-based nanoclusters. It should be noted that other attempts to synthesize 4-bromobenzaldehyde-based Ald-SNPs of the appropriate size and zeta potential for use in single SNP-based nanoclusters in our lab have been successful, and as such they are promising for use in Dox loaded single and dual SNP carrying nanoclusters.

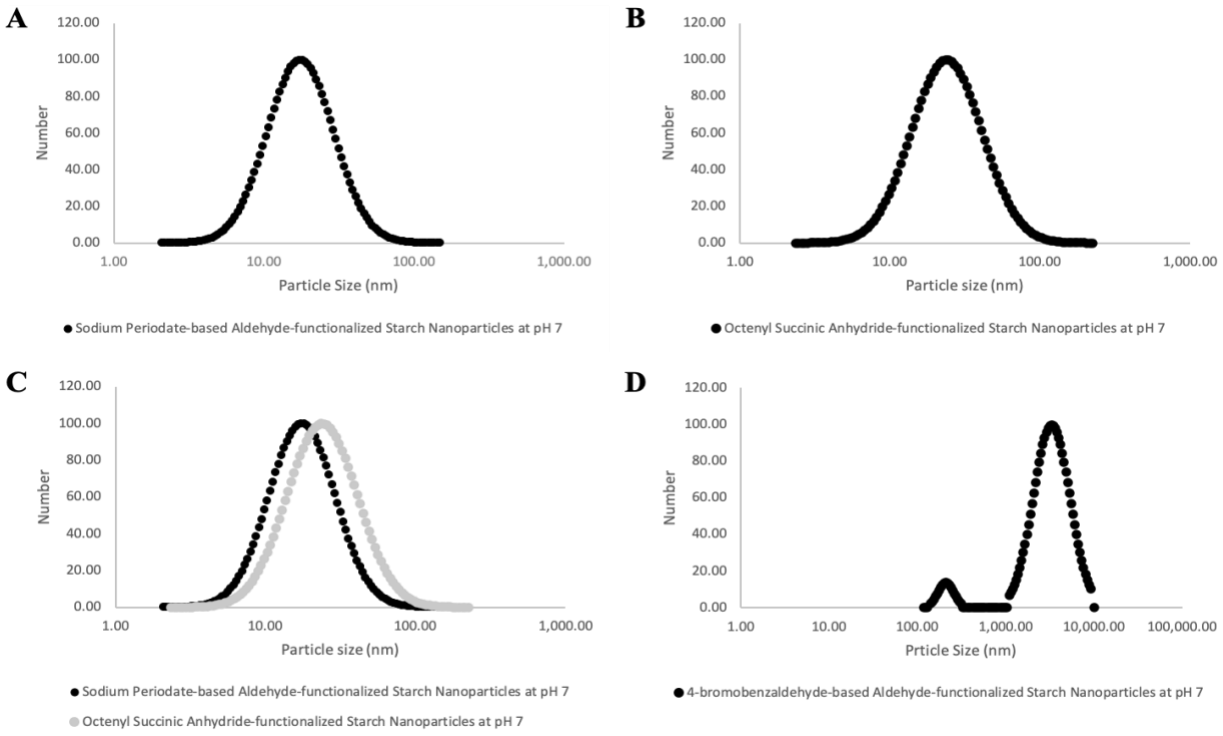

Figure 5: Dynamic light scattering (DLS) number average size distributions of variably functionalized starch nanoparticles (SNPs) at pH 7. (A) The size distribution of sodium periodate ($NaIO_4$)-based aldehyde-functionalized SNPs (Ald-SNPs). (B) The size distribution of octenyl succinic anhydride-functionalized SNPs (OctSAn-SNPs). (C) A comparison of DLS size distributions for $NaIO_4$-based Ald-SNPs and OctSAn-SNPs. (D) The size distribution of 4-bromobenzaldehyde-based Ald-SNPs.

Table 1: Overview of DLS and zeta potential readings of the three variably functionalized SNPs and the POEGMA-Hyd-DMA polymer.

Sample	Mean Particle Size (nm)	Standard Deviation (nm)	Mean Polydispersity	Zeta Potential (mV)
$NaIO_4$-based Ald-SNPs	78	4.54	0.327	12
OctSAn-SNPs	127	5.60	0.367	5
4-bromobenzaldehyde-based Ald-SNPs	2,534	245.59	0.343	N/A[5]
POEGMA-Hyd-DMA (40 µL of TGA)	–	–	–	-7

2.3.2 POEGMA-Hyd-DMA Polymer Characterization

Following the synthesis of the initial POEGMA polymer (POEGMA-AA) with 30 µL of TGA, the M_n and weighted average (M_w) were determined to be approximately 19 kDa and 67 kDa respectively using GPC, as seen in Table 2. While the M_n of this polymer lies within, though at the upper limit of the acceptable range of 15-20 kDa, the M_w slightly exceeds the maximum boundary of 60 kDa for polymers commonly used in nanocluster formations. As well, past experiments have indicated that polymers with M_n less than 40 kDa are ideal for *in vitro* application and lie below the renal clearance threshold. POEGMA-AA synthesized with 40 µL of TGA on the other hand reproducibly generates polymers with M_n and M_w within the acceptable ranges (data unavailable[6], data ranges presented in Table 2). The degree of carboxylic acid functionalization of the POEGMA-AA formed using 30 µL of TGA was determined to be approximately 33 mol% using a method of calculation previously established and tested in the

[5] Data not collected at this time.
[6] Data collected and stored in the Hoare Lab.

Hoare Lab (see Supplementary File 2). This is in line with the theoretical degree of carboxylic acid functionalization determined for POEGMA-AA formed using 30 µL of TGA (33 mol%), and only slightly below that for POEGMA-AA synthesized using 40 µL of TGA (35 mol%). The degree of hydrazide functionalization of the subsequently generated POEGMA-Hyd (formed initially using 30 µL of TGA) was determined to be approximately 14 mol% of the total number of AA groups, again using a method of calculation previously established and tested in the Hoare Lab (see Supplementary File 2). This is substantially lower than the norm for hydrazide functionalization of POEGMA-AA polymers (35 mol%) synthesized in the manner presented in 2.2.4 using 40 µL of TGA. Such a difference in hydrazide functionalization also conflicted with the expectation that functional group conversion was proceeding well based on the detection of a continual rise in pH above 4.75 for more than 4 hours during the reaction with POEGMA-AA, ADH and EDC. This ultimately necessitated the addition of 1.0 M HCl at higher quantities than are usually needed with such low percentage hydrazide functionalizations as was recorded in this case. Given the excessive M_w of the POEGMA-Hyd-DMA polymers made using 30 µL of TGA, polymers synthesized using 40 µL of TGA were examined further exclusively. Moving forward, however, depending on the physical characteristics of dual-SNP loaded nanoclusters, their stability under physiological conditions, and disassembly under acidic conditions, the amount of TGA used (35-45 µL) to generate the POEGMA polymers and the precise degree of functionalization may serve easily manipulated variables to alter polymer, and by extension dual SNP carrying nanocluster size, and nanocluster charge reversal sensitivity respectively.

A zeta potential analysis was also conducted for the POEGMA-Hyd-DMA polymer generated using 40 µL of TGA, which revealed it to possess a potential of approximately -7 as seen in

Table 1. This reading is in line with expectations based on the polymer's Hyd-DMA conjugation and external carboxylic acid group which would be deprotonated in water (pH 7). A negative zeta potential, particularly of this magnitude, also indicates these polymers will be capable of electrostatic interactions with more cationic Ald-SNPs like those synthesized using the method discussed in 2.2.2.1 and presumably those synthesized using the method in 2.2.2.2, as well as the less cationic OctSAn-SNPs synthesized based on the protocol outlined in 2.2.3. Such interactions, however, must be verified experimentally once 4-bromobenzaldehyde-functionalized Ald-SNPs of the proper size and zeta potential have been synthesized. It should be noted that while this study uses zeta potential to assess polymer charge as an indicator of its suitability for use in nanoclusters, this type of assessment is not necessarily accurate. As such, zeta potentials are used here only as a pseudo representation of charge specifically to observe the sign and changes in magnitude of the polymer's potential under varying conditions.

Table 2: Overview of GPC data recorded for POEGMA-AA polymers during POEGMA-Hyd-DMA synthesis.

Volume of TGA Used in POEGMA Synthesis	Mn	Mw	Polydispersity
30 µL	19,000	66,700	3.438
40 µL[7]	15,000-20,000	< 40,000	~2-3

2.3.3 Nanocluster Drug Loading and Theoretical Efficacy

Given the degradation of the $NaIO_4$-based Ald-SNPs during even short-term storage, only 4-bromobenzaldehyde-based Ald-SNPs were examined beyond the preliminary stage for drug loading and use in nanoclusters. Dox quantification in Ald-SNP carrying nanoclusters (single

[7] Data from previous analyses in the Hoare Lab.

SNP nanoclusters) performed alongside the current project has revealed that Dox has between 1-2% loading efficiency (0.01-0.02 grams of Dox per gram of nanocluster). While this may seem minimal, there are two considerations necessary to interpret the potential therapeutic efficacy of such Dox-loaded nanoclusters. First, the effective local concentration for Dox-induced cytotoxicity is 2-10 μM (Smith et al., 2006), which translates to 2-10 nmol/mL. A 1-2% loading efficiency of Dox in a standard sample of Ald-SNP carrying nanoclusters (100 mg/mL) translates to approximately 1.8-3.6 μmol/mL, which is between 1,800 and 3,700 times higher than even the maximum required local effective concentration. This implies that even with 1 mL of a 100 mg/mL Dox-loaded Ald-SNP carrying nanocluster (designed with a 10:90 mass ratio of Ald-SNPs to POEGMA-Hyd-DMA), a significant quantity of Dox is contained and can be delivered to a tumour. The second consideration is that the dose of Dox provided to a patient can be scaled up simply by increasing the concentration or volume of Dox-loaded nanocluster solution administered, which is already less toxic than increasing the use of the free drug itself and ensures a higher proportion of drug delivery directly to tumours.

While the efficiency of Erl loading onto OctSAn-SNPs (Erl-OctSAn-SNPs), and subsequent Erl-OctSAn-SNP loading into nanoclusters have yet to be assessed, these analyses and their results should be preceded by the acknowledgment of several factors. The effective local concentration of Erl necessary for EGFR inhibition is approximately 100 nM (Buck et al., 2006), meaning this drug is 10-100 times more potent than Dox. As such, substantially less of it is required during drug delivery. This likely permits a limited Erl loading efficiency onto OctSAn-SNPs for OctSAn-SNP and dual SNP carrying nanoclusters to remain a suitable method of Erl delivery to tumours. If Erl loading efficiency is comparable to that of Dox, this also means that the mass

ratio of Dox-Ald-SNPs and Erl-OctSAn-SNPs used in nanocluster formation can significantly favour the former (for example, at a 95:5 or 90:10 Ald-SNP:OctSAN-SNP mass ratio combination) in dual SNP carrying nanoclusters. While some Dox-Ald-SNPs loading efficiency in these nanoclusters would be sacrificed for Erl-OctSAn-SNP loading, it is expected that the synergistic effect from the combination of Dox and Erl would ultimately increase the therapeutic efficacy of these dual SNP carrying nanoclusters compared to Dox-Ald-SNP carrying nanoclusters at an equivalent nanocluster dose (assuming sufficient drug release from both SNP variants). As well, if necessary, more dual-SNP nanoclusters could be added in a sample to equate the Dox dose to that of Dox-Ald-SNPs nanoclusters which should at minimum maintain the drug's apoptotic effect.

When examining literature surrounding the synergistic effects of Dox and Erl, two factors become clear with regard to the timing and sequence of drug delivery. In terms of the time-dependency of drug administration, it has been found that Erl must be administered at least 4 hours prior to Dox for synergism to occur, and that maximum synergy is observed when Dox is administered 24 hours following Erl (Lee et al., 2012). In the case of dual SNP carrying nanocluster-based drug delivery, this would necessitate the sequential release of Erl-OctSAn-SNPs, followed by the Dox-Ald-SNPs some hours later in order for synergism between the two drugs to occur. Based on the SNP and polymer zeta potentials listed in Table 1, there lies the possibility that if weaker electrostatic interactions are observed between the POEGMA-Hyd-DMA and Erl-OctSAn-SNPs compared to the Dox-Ald-SNPs in dual SNP carrying nanoclusters, then Erl will be delivered to tumours prior to Dox due to earlier OctSAn-SNP release during nanocluster disassembly. Furthermore, previous analyses of nanoclusters carrying only Ald-

SNPs have revealed that they do not immediately undergo disassembly when exposed to an acidic environment equivalent to that of a tumour's microenvironment, and in fact require more than 24 hours to disassemble (Supplementary Figure 1A-C). This indicates the potential for dual SNP carrying nanoclusters to release Erl-OctSAn-SNPs earlier than Dox-Ald-SNPs with a time delay long enough to allow for substantial synergistic cancer killing *in vitro* and *in vivo*. Finally, a necessity of the synergistic cancer killing between Dox and Erl is sustained EGFR inhibition by Erl. In terms of dual SNP carrying nanocluster delivery, this may also be achieved based on the progressive disassembly of nanoclusters releasing Erl-OctSAn-SNPs over time prior to and in concert with Dox-Ald-SNPs. It should be noted that while there may not be a 24-hour delay in successive Erl-OctSAn-SNP and Dox-Ald-SNP release from nanoclusters, continual SNP and consequent drug release could theoretically generate a synergistic effect as early as 4 hours following the start of nanocluster disassembly if sufficient concentrations of both Dox and Erl are reached. A maximum synergistic effect may then be observed either after 24 hours of sustained release, or when maximum drug concentrations from nanocluster delivery are reached - should those be lower than their optimal concentrations (Lee, et. al, 2012).

Another interesting aspect of OctSAn-SNP-based Erl delivery to tumours is that following nanocluster disassembly and Erl-OctSAn-SNP release, the nearly neutral charge of these SNPs may direct them more towards tumour penetration than cancer cell membrane binding. This is somewhat opposed to what might be expected with the Dox-Ald-SNPs that are more likely to be targeted towards binding to the negative cancer cell membranes due to their higher cationic charge. Whether this variable SNP targeting for either tumour penetration (Erl-OctSAn-SNPs) or cancer cell membrane interactions (Dox-Ald-SNPs) supports or hinders synergistic cancer killing

based on the location of drug release remains to be determined, and it is likely that 3D assays, such as a spheroid model, will be useful for assessing this particular characteristic of dual SNP carrying nanocluster-based drug delivery.

2.3.4 Considerations for Future Dual Starch Nanoparticle Carrying Nanocluster Evaluation

In order to begin the formation of dual SNP carrying nanoclusters, an evaluation of OctSAn-SNP stability must be conducted under physiological and acidic conditions. For these analyses, OctSAn-SNP samples should be tested that have been synthesized immediately prior to testing and have been allowed to remain in storage for a prolonged period of time to determine if these SNPs undergo untimely structural degradation as was the case with the $NaIO_4$-based Ald-SNPs. Similar analyses should also be conducted to confirm the stability of 4-bromobenzaldehyde-based Ald-SNPs as well. Once stabilities have been confirmed, drug loading efficiency of both the Ald-SNP and OctSAn-SNP variants can be determined, followed by an assessment of individual and tandem loading into nanoclusters. From there, the ratio of Dox-Ald-SNPs and Erl-OctSAn-SNPs necessary to achieve sufficient concentrations of both drugs for synergistic cancer killing can be determined, and a protocol for therapeutically effective dual SNP carrying nanoclusters can be fully elucidated. Following these experiments, stability and disassembly analysis of dual SNP carrying nanoclusters would need to be conducted to verify nanocluster integrity during circulation and the sequence and time dependence of Ald- and OctSAn-SNP release during disassembly. Further analysis and quantification of drug release from SNPs after nanocluster disassembly may also be conducted to determine the actual therapeutic potential of these nanoclusters. This information will ultimately reveal if further structural modifications are

necessary for dual SNP carrying nanoclusters and guide the investigation of the therapeutic efficacy of such nanoclusters based on synergistic drug delivery *in vitro* using 2D and 3D cell assays and *in vivo* using a transgenic mouse model.

2.4 Conclusion

Here, a preliminary assessment is provided for the suitability of 4-bromobenzaldehyde-based cationic Ald-SNPs and hydrophobized cationic OctSAn-SNPs to be used for Dox- and Erl-loading respectively and in combination with POEGMA-Hyd-DMA polymers for the formation of multi-drug loaded dual SNP carrying nanoclusters. The complex and multifaceted process of single SNP carrying nanocluster-based drug delivery has previously been shown to provide a suitable means of overcoming the physiological barriers that commonly restrict NP-based drug delivery. A design for Dox-Ald-SNP and Erl-OctSAn-SNP carrying nanoclusters presents a novel method for synergistic drug delivery and is likely to well surpass the efficacy of its Dox-Ald-SNP-loaded predecessor. The material characterizations performed thus far, as well as the implications of their characteristics, functionalities, and drug-loading abilities suggests that 4-bromobenzaldehyde-based Ald-SNPs and OctSAn-SNPs are certainly acceptable to be tested further and utilized alongside POEGMA-Hyd-DMA for synthesizing dual SNP loaded nanoclusters.

The loading of two or more synergistic drug-carrying SNP variants into nanoclusters poses new challenges to cluster formation and may necessitate some structural modifications to ensure integrity during circulation and appropriate disassembly and SNP release at the site of tumours to achieve synergistic cancer killing. In terms of the polymers used in nanoclusters, this may entail

changes in length and the extent or type of functionalization. In terms of the SNPs, this may require changes in the extent or type of functionalizations of one or both SNP variants to ensure that each possesses physical and chemical characteristics that allow them to sufficiently load drugs independently and be loaded together into nanoclusters at effective concentrations. Ultimately, synthesizing dual SNP carrying nanoclusters loaded with an appropriate quantitative ratio of synergistic drugs can be expected to prove invaluable for improving chemotherapeutic-based treatment of tumours throughout the body. Thus, efforts to formulate such a design must persist in order to strengthen the regimen of treatments available for tumours, and it is imperative that further investigations into similar NP-based therapeutics be conducted to combat cancer as the number of new diagnoses and cancer-related deaths continues to rise both in Canada, and worldwide.

PART 3: FUTURE DIRECTIONS

3.1 Introduction

In light of the data presented and discussed above, additional experiments must be conducted to assess the viability of using Ald- and OctSAn-SNPs alongside POEGMA-Hyd-DMA for the synthesis of dual SNP carrying nanocluster capable of synergistic drug delivery. The following sections present protocols for several experiments that are required prior to and once dual SNP carrying nanoclusters have been synthesized to evaluate their drug loading efficiency, stability, disassembly, and therapeutic efficacy. An alternative hydrophobized SNP synthesis protocol is also presented that was not previously investigated but may also be examined experimentally in the future for use in dual SNP carrying nanoclusters. A discussion of the anticipated results of SNP and nanocluster experiments is provided, and where possible data from previously examined Ald-SNPs and Ald-SNP carrying nanoclusters will be used as a reference for experimental analyses. Potential means of troubleshooting or otherwise addressing potential issues that might arise during experimental SNP and nanocluster analysis are also briefly outlined. Finally, this section concludes with some general comments on the work developing dual SNP carrying nanoclusters for synergistic tumour therapy thus far and its potential for future clinical application.

3.2 Materials and Methods

3.2.1 Materials

Succinic anhydride (SAn, ≥99%) was obtained from Sigma Aldrich (Oakville, ON). Dulbecco's modified Eagle's medium (DMEM), fetal bovine serum (FBS) and 1% penicillin were obtained from Invitrogen. All chemicals were used as received.

3T3 *Mus musculus* mouse fibroblast cells were obtained from ATCC Cedarlane Laboratories (Burlington, ON) and cultured in DMEM supplemented with 10% FBS and 1% penicillin streptomycin (PS); all of which were received from ThermoFisher Scientific. Trypsin-ethylenediamine tetraacetic acid (EDTA) and calcein AM/ethidium homodimer live/dead assay kits were obtained from Invitrogen.

3.2.2 Alternate Hydrophobized Starch Nanoparticle Formulation

An alternative method of adding an anhydride group onto SNPs to the one discussed in 2.2.3 is through the use of SAn. Outlines that present manipulations of both this and the 2.2.3 SNP synthesis protocols have been previously designed by the Hoare Lab (see Supplementary Files 4 and 5).

3.2.2.1 Synthesis of Succinic Anhydride-functionalized Starch Nanoparticles

To begin generating the SAn-functionalized SNPs (SAn-SNPs), a 100 g aqueous dispersion of cationic SNPs (5% w/v in MQW) inside a 250 mL round-bottomed flask was mixed with 0.073 g of $NaHCO_3$ and placed under magnetic stirring. The pH of the solution was monitored for 1 hour using a pH probe and kept between 9-10 by adding 1.0 M NaOH as required. 0.309 g of SAn was then added dropwise over the course of 1 hour while a pH of 9-10 was maintained. The pH was monitored for an additional 30 minutes before the sample was neutralized to pH 7 with the addition of 1.0 M HCl. The SAn-SNPs were then dialyzed against MQW over 6 x 12 dialysis cycles using a 3.5−5 kDa molecular weight cut-off membrane and lyophilized to dryness for storage.

3.2.3 Acidifying Starch Nanoparticle Samples

To determine SNP stability under acidic conditions, SNP solutions of 100 mg/mL in MQW were prepared (2-4 mL per sample), vortexed for 20 seconds, and subsequently placed in an incubator for 24 hours at room temperature. Samples were then centrifuged at 10,000 RPM for 10 minutes at 20 °C. The supernatants were then transferred to a new 15 mL Falcon tube, and the pellets (consisting of SNP aggregates) were discarded. The pH of the solution was then lowered to 6.4-6.8 with the addition of 0.1 HCl as required and SNPs had their size and zeta potentials measured.

3.2.4 Starch Nanoparticle Drug Loading

Given that drug loading was only assessed above in the context of Dox loading into Ald-SNP carrying nanoclusters, it is important to assess the drug loading efficiency of Dox and Erl onto Ald- and OctSAn-SNPs respectively and into nanoclusters following SNP mixing with POEGMA-Hyd-DMA. The protocol for generating Dox-Ald-SNPs is provided in 2.2.7.

3.2.4.1 Quantification of Doxorubicin Loaded onto Aldehyde-functionalized Starch Nanoparticles

In order to quantify the amount of Dox loaded onto the Ald-SNPs, solid Dox-Ald-SNPs were dissolved to generate a 2 mg/mL solution. Dox concentration was then measured using fluorescence intensity (emission signal at 595 nm upon excitation with a 470 nm laser) and determined using a standard curve.

3.2.4.2 Erlotinib Loading onto Octenyl Succinic Anhydride-functionalized Starch Nanoparticles

To prepare Erl loaded SNPs, OctSAn-SNPs were dissolved at 10 wt% in MQW, and Erl was prepared at a concentration of 10 mg/mL in DMSO. The OctSAn-SNP and Erl solutions were mixed at a mass ratio of 10:1 OctSAn-SNP:Erl in a 250 mL round-bottomed flask and left to stir for 24 hours. The solution was then dialyzed against MQW over 6 x 12 dialysis cycles using a 3.5−5 kDa molecular weight cut-off membrane and lyophilized to dryness for storage.

3.2.4.3 Quantification of Erlotinib Loaded onto Octenyl Succinic Anhydride-functionalized Starch Nanoparticles

There is currently no established protocol known for quantifying the efficiency of loading Erl onto OctSAn-SNPs, or any equivalent gel-like nanoparticle systems, however there have been a number of investigations that have sought to develop highly specific and sensitive means of quantifying Erl in human plasma. Therefore, protocols from such works may be adapted to be used for both Erl loading efficiency onto SNPs and in single and dual SNP carrying nanoclusters. One method for quantifying Erl in solution has been described by Svedberg et al. (2015), which involved the implementation of liquid chromatography tandem mass spectrometry (MS). A potential issue with this method, however, is that it is challenging to conduct routinely, and as such Zhang et al. (2005) developed a means of quantifying Erl in solution using reverse phase high-performance liquid chromatography (HPLC) with ultraviolet (UV) detection. Other researchers have also adapted the method used by Zhang et al. (2005) by replacing the use of UV detection with MS. Based on these various works and their successful Erl quantification, it is likely that a method of HPLC coupled with MS can be used to evaluate Erl loading efficiency

onto OctSAn-SNPs (or other hydrophobized SNPs) as well as into single or dual SNP carrying nanoclusters.

3.2.5 Dual Starch Nanoparticle Carrying Nanocluster Formation

To start, both Ald- and OctSAn-SNPs were dissolved in 15 mL Falcon tubes with MQW to generate material concentrations of 100 mg/mL. POEGMA-Hyd-DMA was also dissolved in a 15 mL Falcon tube using 1.0 M NaOH, again to generate a material concentration of 100 mg/mL. Samples were then centrifuged at 10,000 RPM for 10 minutes at 20 °C, after which the supernatants were transferred to 20 mL glass wells and the pellets (consisting of SNP or polymer aggregates) were discarded. In these nanoclusters, a 10:90 mass ratio of SNPs to POEGMA-Hyd-DMA was used. Generally, 0.9 mL cumulatively of both SNP variant supernatants (different volumes for different mass ratio combinations of SNPs) along with 8.1 mL of POEGMA-Hyd-DMA supernatant was added to a 20 mL glass sample jar. All samples were subsequently kept under high magnetic stirring for 24 hours before storage at 4 °C. Dox-loaded nanoclusters were mixed in the absence of light.

3.2.6 Nanocluster Stability and Disassembly Evaluation

Following dual SNP carrying nanocluster synthesis, nanocluster samples were added to separate 12 kDa dialysis bags and sealed using removable clips. These bags were then placed in 100 mL beakers and submerged in 80 mL of MQW. To assess nanocluster stability, samples underwent dialysis against MQW, with water being changed twice a day for the duration of observation. To assess nanocluster disassembly, samples underwent dialysis against MQW that was acidified

using 0.1 M HCl to achieve a pH of 6.4-6.8, with water being changed and re-acidified twice a day for the duration of observation.

3.2.6.1 Particle Size Analysis of Nanoclusters

The sizes of nanoclusters were determined using the same technical specifications as were used for SNP readings. Prior to DLS analysis, 0.5 mL of a nanocluster solution was removed from the sample's dialysis bag and added a 10 mm cuvette along with 1.5 mL of MQW. All samples underwent mixing by inversion 5 times before being analyzed. Nanocluster readings were examined using the 'MSD' and 'intensity' outputs.

3.2.6.2 Zeta Potential Measurements of Nanoclusters

The zeta potentials of nanoclusters were determined using the same technical specifications as were used for SNP and POEGMA-Hyd-DMA readings. Prior to zeta potential readings, 1 mL of a nanocluster solution was removed from the sample's dialysis bag and added a 10 mm cuvette along with 0.5 mL of a 5 mM NaCl solution and underwent mixing by inversion 5 times. Zeta potential outputs were again analyzed using the Smoluchowski zeta potential model.

3.2.7 Quantification of Erlotinib Loading in Octenyl Succinic Anhydride-functionalized Starch Nanoparticle Carrying Nanoclusters

The quantification of Erl loading in OctSAn-SNP carrying nanoclusters either by itself or in combination with Dox-Ald-SNPs is likely to be performed in the same manner as the quantification of Erl loading onto OctSAn-SNPs described in 3.2.4.3.

3.2.8 Quantification of Drug Release from Nanoclusters

To quantify the amount of drug released from nanoclusters, a comparison can be done between free drug found in the water used to dialyze nanocluster samples and pellets of nanoclusters obtained following sample centrifugation at 10,000 RPM for 10 minutes at 20 °C, supernatant removal, and nanocluster resuspension in MQW. Quantification would be done based on the method discussed in 2.2.9 and a protocol adapted from previous works discussed in 3.2.4.3. for Dox and Erl respectively.

3.2.9 Cell Preparation and Passage

The methods described below for preparing media, defrosting and culturing cells new cells, performing cell passages, and counting cells follow the protocols previously designed by the Hoare Lab (see Supplementary File 6).

3.2.9.1 Media Preparation

To prepare the cell media, 445 mL of DMEM, 50 mL FBS (10% of overall volume), and 5 mL penicillin-streptomycin (1% of total volume) were added to a storage flask and mixed by pipetting the solution up and down multiple times.

3.2.9.2 Defrosting and Culturing New Cells

Briefly, 10 mL of fresh warmed media was added to a flask. A vile of cells was removed from the liquid nitrogen storage unit, and the bottom of the vile was submerged in a 37 ℃ water bath for 1-3 minutes. Defrosting progress was checked by removing the vial from the water and flipping the vial upside down. Once only a small chunk of ice remained, cells were quickly

transferred to the flask containing the 10 mL of media. The flask was then placed in an incubator at 37 ℃. Cells were monitored daily for health and confluence.

3.2.9.3 Cell Passage

Briefly, cell flasks were removed from the incubator and checked for media colour change and under a microscope for confluence. Prior to passage, PBS, DMEM, were warmed in a 37 ℃ water bath. First, old media was removed from cell flasks and discarded. 10 mL of PBS was then added to flasks to rinse cells and was subsequently discarded. 2-3 mL of trypsin was then added to flasks and moved around to cover all cells. The flasks were subsequently returned to the incubator for 2-3 minutes. Flasks were then removed from the incubator again and tapped gently to promote cell detachment, which was confirmed using a light microscope. Following this, 10 mL of DMEM was added to neutralize the effect of trypsin on the cells. The media from each flask was then transferred to a 15 mL Falcon tube and centrifuged at 500 RPM for 5 minutes. The media from each Falcon tube was discarded, leaving only cell pellets. 10 mL of media was added to the 15 mL Falcon tube containing the pellet, along with 1 mL of DMEM which was pipetted up and down multiple times to resuspend the cells. 40 µL of the resuspended cell solution was then added to a new Falcon tube containing 10 mL of media and mixed by pipetting up and down. Both the new cell suspensions were then added to separate flasks and stored in the incubator. Cells were checked daily or every other day and passaged twice a week.

3.2.9.4 Cell Counting Protocol

Cell counting was performed during cell passage prior to the cell suspensions being transferred from their 15 mL Falcon tubes to new flasks for incubation. Briefly, 10% dilutions were

performed by adding 90 µL of DMEM and 10 µL of cell suspension to an Eppendorf tube, which underwent mixing by pipetting the solution up and down. 10 µL of this diluted mixture was then added to each side of a hemocytometer. The hemocytometer was then observed under 10X magnification, and cells were counted in one quadrant. The total number of cells was determined by taking the number of cells counted and multiplying it by 10^4 to account for dilutions.

3.2.10 Cytotoxicity Assays

Both 2D and 3D cell spheroid assays should be used to assess nanoclusters *in vitro*. The 2D cell assay described below is adapted from Zhou et al. (2019), and the spheroid assay is adapted from Mittler et al. (2017).

3.2.10.1 2D Cytotoxicity Assay and Analysis

Briefly, cultured cells were seeded into 96-well plates at a density of 5000 cells per well and incubated at 37 ℃. The growth media was replaced with fresh media after 24 hours. Following this, control (free drug) and nanocluster samples were added into their designated wells. Cells were cultured for 24-72 hours. Cell cytotoxicity was determined using CCK-8 assays. The absorbance of each well was measured using an ELISA plate reader at a test wavelength of 450 nm, and cell growth inhibition was calculated as per the protocol outlined by Zhou et al. (2019):

$$Cell\ Viability\ (\%) = \frac{I_{sample} - I_{blank}}{I_{control} - I_{blank}} \times 100\%$$

where I_{sample} and $I_{control}$ represent the intensity determined for cells treated with different samples and for control cells respectively.

3.2.10.2 Cell Spheroid Assay and Cytotoxicity Analysis

The method for generating cell spheroids described here is based on the 'hanging drop' method outlined by Mittler et al. (2017). Briefly, to prepare the cell suspension, cell monolayers were washed with 10 mL of PBS and treated with 1.5 mL of a trypsin–EDTA solution prior to being incubated for 5 minutes. At this time, 8 mL of media was added to neutralize the trypsin, and the cell suspensions were centrifuged at 1000 RPM for 5 minutes. Following supernatant removal, cell pellets were resuspended with the media at the density of 100000 cells/mL. 10 µL of the cell suspensions was dropped onto the lids of the petri dishes and incubated at 37 ℃. After 1-2 weeks, the cell spheroids were determined to be ready appropriate for use as the *in vitro* tumor model to examine tumour penetration by SNPs. Drug-loaded nanoclusters could subsequently be added to the medium of cell spheroids, after which cells remained in culture for 3-48 hours. The spheroids were then washed with PBS and fluorescent images at different depths were taken using confocal microscopy.

3.3 Expected Results

3.3.1 Expected Use of Hydrophobized Starch Nanoparticle Variants in Dual Starch Nanoparticle Carrying Nanoclusters

The OctSAn-SNPs described in 2.3.1 are expected to maintain their structural integrity both under physiological conditions as seen in Figure 1B and in acidic conditions similar to the $NaIO_4$-based Ald-SNPs tested previously (Supplementary Figure 2). Some evidence for OctSAn-SNP stability under physiological conditions already exists since these SNPs were observed to

have the same DLS readings in MQW at a pH of 7 immediately and several hours after mixing (data unavailable[8]).

While the OctSAn-SNPs show great promise for use as the hydrophobized Erl-loading SNPs in Dox- and Erl-loaded dual SNP carrying nanoclusters, alternative methods of synthesizing SNPs with anhydride functionalizations exist, of which one – the SAn SNP functionalization method – is likely to produce anhydride-functionalized SNPs similar to the OctSAn-SNPs based on prior analyses in the Hoare lab (see Supplementary File 5). Such alternative methods of synthesizing hydrophobized SNPs can be examined either as a replacement for OctSAn-SNPs should they ultimately prove insufficient for use in dual SNP carrying nanoclusters. Alternatively, they may also offer a variety of nanocluster formulations to better improve the clinical therapeutic benefit of dual SNP carrying nanoclusters depending on specific requirements of a patient's diagnosis (if for example alternative combinations of chemotherapeutic drugs to Dox and Erl may improve treatment efficacy).

3.3.2 Expected Nanocluster Stability and Disassembly

Based on previous assessments of Ald-SNP carrying nanoclusters, and assuming minimal interference between the Ald- and OctSAn-SNPs, it is expected that dual SNP carrying nanoclusters would remain stable under physiological conditions and circulate effectively in the blood stream. A similar change in nanocluster zeta potentials between physiological and acidic conditions would also be expected for dual SNP carrying nanoclusters compared to previously examined Ald-SNP carrying clusters given they both use the POEGMA-Hyd-DMA polymer (Supplementary Tables 1 and 2). Under acidic conditions, however, it is possible that the dual

[8] Data collected and stored in the Hoare Lab.

SNP carrying nanoclusters would disassemble more readily than Ald-SNP carrying nanoclusters since the more hydrophobic, or less positively charged Erl-SNPs require less of a change in polymer charge to lose their electrostatic attraction within the clusters. This may lead to nanocluster disassembly earlier than, or more shortly after 24 hours post exposure to an acidic environment than was previously seen with Ald-SNP carrying nanoclusters (Supplementary Figure 1A-C).

It is important to note that while SNPs not loaded with drugs are favoured for initial stability and disassembly assessments, drug binding to SNPs may affect their loading into nanoclusters as well as overall nanocluster stability and disassembly. As such, rounds of drug-loaded nanocluster examinations should be conducted to verify their stability under physiological conditions and disassembly under more acidic conditions prior to *in vitro* and *in vivo* testing.

3.3.3 Expected Starch Nanoparticle and Nanocluster Drug Loading Efficiency

Based on the protocols for nanocluster synthesis, it is expected that Dox loading onto Ald-SNPs is greater than the 2% loading efficiency determined for this drug's final loading efficiency into Ald-SNP carrying nanoclusters since not all Ald-SNPs embed themselves during cluster formation. SNP loading efficiency, however, is ultimately far less telling of a nanocluster's therapeutic potential, and as such can be considered as a preliminary means of estimating a nanocluster's final drug loading efficiency. Further investigations into improving Dox loading onto Ald-SNPs based on their functionalization, as well as SNP loading into nanoclusters based on electrostatic interactions (possibly by raising the magnitude of charge difference) may yield improved efficiencies for both stages of Dox loading.

At this time, Erl loading efficiency has not been measured for either OctSAn-SNPs or nanoclusters, and despite the use of the same drug and nanocluster loading protocols as with Dox and Ald-SNPs, a lack of literature or previous work surrounding Erl loading onto gel-like nanoparticles or SNPs prevents an accurate prediction for such efficiencies from being made. Should, however, Erl loading efficiencies be similar to or below that of Dox and Ald-SNPs, it would be of less concern since the former's effective local concentration is much lower. Given the expected suitable interactions between Ald-SNPs and OctSAn-SNPs with POEGMA-Hyd-DMA, and similar loading efficiencies of drugs into dual SNP carrying nanoclusters, it likely that the loading protocol for SNPs into the nanoclusters will greatly favour the Dox loaded Ald-SNPs.

Depending on the loading efficiency of Erl into OctSAn-SNP carrying nanoclusters, varying ratios of Erl-loaded OctSAn-SNPs and Dox-loaded Ald-SNPs can be mixed together to determine final nanocluster loading efficiency. From here, a quantification of the total amount of both Erl and Dox inside dual SNP carrying nanoclusters can be examined, followed by an assessment and quantification of drug release to determine if enough of both drugs are delivered to achieve a therapeutic and synergistic effect *in vitro* and *in vivo*. The idea here would be to generate and test nanoclusters carrying predominantly Dox-loaded Ald-SNPs that maximize cancer cell DNA damage along with a smaller proportion of the Erl bound to OctSAn-SNPs to unmask pro-apoptotic pathways. Initial ratios to be tested may range from 95:5 to 80:20 Dox-Ald-SNPs to Erl-OctSAn-SNPs, where volumes of each SNP variant correspond to their percent representation in the mass ratio combination used in a particular experimental trial multiplied by 0.9 mL – the allotted volume of SNPs in 10:90 SNP:POEGMA-Hyd-DMA nanoclusters. For

example, in a 95:5 Ald-SNP:OctSAn-SNP mass ratio trial, 0.855 mL and 0.0045 mL of Ald-SNP and OctSAn-SNP supernatants respectively would be added to 1.8 mL of POEGMA-Hyd-DMA supernatant to generate the dual SNP carrying nanoclusters.

3.3.4 Expected Nanocluster Cytotoxicity

Previous assessments of Dox-Ald-SNP carrying nanoclusters have revealed that this method of drug delivery can indeed provide a therapeutic benefit *in vitro* and *in vivo*. The increased efficacy of these nanoclusters carrying two synergistic drugs is heavily dependent on the sequence and time delay between Erl-OctSAn-SNP and Dox-Ald-SNP release. Given Erl's effective local concentration, and assuming similar loading efficiency to Dox, it can be expected that dual SNP carrying nanoclusters predominantly embedded with Dox-loaded Ald-SNPs will be able to demonstrate a synergistic effect to some extent during the course of treatment regardless of sequence or specific time of SNP and subsequent drug release. Should nanoclusters disassemble over the span of several hours, synergism between Dox and Erl may be observed as early as 4 hours post administration *in vitro*, with efficacy gradually increasing over the course of nanocluster disassembly with increased Dox-Ald-SNP release. If nanoclusters can be synthesized such that Erl-OctSAn-SNPs are released closer to the initial cluster exposure to acidic conditions, then the 24 hour or longer delay in nanocluster disassembly observed previously (Supplementary Figures 1A-C) may allow for maximum synergy between Dox and Erl (Lee et al., 2012), and an increase in Dox-based cancer cell death of approximately 2-fold in 2D cell assays (Morton et al., 2014). As well, given the expected gradual disassembly of nanoclusters, it is likely that both drugs will be released gradually, and therefore sustained ERGR inhibition will be present during Dox-based cancer killing, ensuring chemotherapeutic synergy.

While several studies investigate the use of NP-based multi-drug delivery using cell spheroid assays, none of the NPs examined are comparable to the gel-like nanocluster system. Despite this, it can still be expected that nanocluster-based multi-drug delivery will improve cytotoxicity in tumour cell spheroids, particularly if deep tumour penetration is achieved for both SNP variants simultaneously, by generating a synergistic effect that spans both the exterior and interior regions of tumour spheroids. This penetrating synergistic effect specifically has important implications for *in vivo* tumour treatment as well.

3.3.5 Contingencies

Despite the expectations that Ald- and OctSAn-SNPs can be successfully used together to generate dual SNP carrying nanoclusters with POEGMA-Hyd-DMA based on preliminary material characterizations, there still lies the potential for their combination to destabilize nanoclusters. SNPs themselves are extremely versatile and can be synthesized in a variety of ways to achieve variations with either minutely or vastly different physical properties like size or charge, as well as different functionalizations. The POEGMA-Hyd-DMA polymer used in nanocluster formation also presents a range of opportunities for modification in terms of size, charge, and functionalization based on its multi-stage synthesis. Combinations of modifications to both the SNPs and the POEGMA polymers therefore provide a rich source of variables that can be altered in the interest of addressing any of the potential physical or physiological challenges that arise with nanocluster-based drug delivery.

Should the combination of Ald-and OctSAn-SNPs not provide an effective means of delivering both Dox and Erl to tumours inside dual SNP carrying nanoclusters, there exists the potential for

other SNP combinations to be explored for such nanocluster formation. If in fact Dox and Erl do not demonstrate synergy *in vitro* despite appropriately timed release of drug-loaded Ald- and OctSAn-SNPs, one explanation may be that this particular combination of chemotherapeutic agents is less effective against the cell type used, in this case the 3T3 Mus musculus mouse fibroblast cells, either in 2D or cell spheroid 3D assays. This may be reasonable to assume, given suitable drug-loaded SNP delivery, since studies suggest that certain combinations of chemotherapeutic drugs demonstrate varying levels of synergy depending on the cell type treated *in vitro* and the tumour type treated *in vivo* (Morton et al., 2012). Based on this, certain cancer cell lines, such as BT-20 cells, should be selected for future *in vitro* nanocluster treatment analyses where synergy is expected and can be confirmed using free drug trials. If in fact synergism is observed with free drug administration but is absent for nanocluster treatments, then a re-evaluation of SNP variant loading ratios would likely be necessary along with improvements in the ability of SNPs to release drugs once at the site of a tumour based on redesigned SNP functionalizations.

3.4 Conclusion

The use of OctSAn-SNPs investigated here represents the analysis of only a single variation of hydrophobized SNP created with the goals of loading the chemotherapeutic Erl and being used in dual SNP carrying nanoclusters. It is likely that further work with nanoclusters will entail the design of new and more diverse SNPs with unique characteristics allowing for improved Erl-loading, or suitable loading of other chemotherapeutic drugs for dual SNP carrying nanocluster-based drug delivery. While maximum synergy is ideal for nanocluster therapy, efforts to design dual SNP carrying nanoclusters are not likely to be in vain even if their therapeutic efficacy falls

short of this goal. Should nanoclusters be designed that can safely and effectively transport multiple drugs to tumours, it is likely that some level of increased cancer killing will occur, whether that be with the combination of Dox and Erl or other chemotherapeutic combinations. Further work on synthesizing nanoclusters capable of the controlled and variable release of SNP variants under acidic conditions, and expansion of the dual SNP carrying nanocluster design is therefore crucial for enhancing nanocluster-based cancer therapy and supporting its clinical application.

References

Allison, M., 2012. Reinventing clinical trials. *Nature Biotechnology*, 30(1), pp.41-49.

Alvarez, R., Musteanu, M., Garcia-Garcia, E., Lopez-Casas, P., Megias, D., Guerra, C., Muñoz, M., Quijano, Y., Cubillo, A., Rodriguez-Pascual, J., Plaza, C., de Vicente, E., Prados, S., Tabernero, S., Barbacid, M., Lopez-Rios, F. and Hidalgo, M., 2013. Stromal disrupting effects of nab-paclitaxel in pancreatic cancer. *British Journal of Cancer*, 109(4), pp.926-933.

Angius, F. and Floris, A., 2015. Liposomes and MTT cell viability assay: An incompatible affair. *Toxicology in Vitro*, 29(2), pp.314-319.

Anselmo, A. and Mitragotri, S., 2016. Nanoparticles in the clinic. *Bioengineering & Translational Medicine*, 1(1), pp.10-29.

Aslantürk, Ö., 2018. In Vitro Cytotoxicity and Cell Viability Assays: Principles, Advantages, and Disadvantages. *Genotoxicity - A Predictable Risk to Our Actual World*.

Azzi, S., Hebda, J. and Gavard, J., 2013. Vascular Permeability and Drug Delivery in Cancers. *Frontiers in Oncology*, 3.

Bae, K., Chung, H. and Park, T., 2011. Nanomaterials for cancer therapy and imaging. *Molecules and Cells*, 31(4), pp.295-302.

Bahrami, B., Hojjat-Farsangi, M., Mohammadi, H., Anvari, E., Ghalamfarsa, G., Yousefi, M. and Jadidi-Niaragh, F., 2017. Nanoparticles and targeted drug delivery in cancer therapy. *Immunology Letters*, 190, pp.64-83.

Barnhart, B., Alappat, E. and Peter, M., 2003. The CD95 Type I/Type II model. *Seminars in Immunology*, 15(3), pp.185-193.

Baek, N., Seo, O., Kim, M., Hulme, J. and An, S., 2016. Monitoring the effects of doxorubicin on 3D-spheroid tumor cells in real-time. *OncoTargets and Therapy*, Volume 9, pp.7207-7218.

Buck, E., Eyzaguirre, A., Haley, J., Gibson, N., Cagnoni, P. and Iwata, K., 2006. Inactivation of Akt by the epidermal growth factor receptor inhibitor erlotinib is mediated by HER-3 in pancreatic and colorectal tumor cell lines and contributes to erlotinib sensitivity. *Molecular Cancer Therapeutics*, 5(8), pp.2051-2059.

Canadian Cancer Statistics Advisory Committee. Canadian Cancer Statistics 2019. Toronto, ON: Canadian Cancer Society; 2019. Available at: cancer.ca/Canadian-Cancer-Statistics-2019-EN (accessed February 25, 2020).

Cabral, H., Matsumoto, Y., Mizuno, K., Chen, Q., Murakami, M., Kimura, M., Terada, Y., Kano, M., Miyazono, K., Uesaka, M., Nishiyama, N. and Kataoka, K., 2011. Accumulation of sub-100 nm polymeric micelles in poorly permeable tumours depends on size. *Nature Nanotechnology*, 6(12), pp.815-823.

Cardone, R., Casavola, V. and Reshkin, S., 2005. The role of disturbed pH dynamics and the Na+/H+ exchanger in metastasis. *Nature Reviews Cancer*, 5(10), pp.786-795.

Carmeliet, P., 2000. Mechanisms of angiogenesis and arteriogenesis. *Nature Medicine*, 6(4), pp.389-395.

Chen, B., Dai, W., He, B., Zhang, H., Wang, X., Wang, Y. and Zhang, Q., 2017. Current Multistage Drug Delivery Systems Based on the Tumor Microenvironment. *Theranostics*, 7(3), pp.538-558.

Chen, B., Wang, Z., Sun, J., Song, Q., He, B., Zhang, H., Wang, X., Dai, W. and Zhang, Q., 2016. A tenascin C targeted nanoliposome with navitoclax for specifically eradicating of cancer-associated fibroblasts. Nanomedicine: *Nanotechnology, Biology and Medicine*, 12(1), pp.131-141.

Chen, W., Li, F., Tang, Y., Yang, S., Li, J., Yuan, Z., Liu, Y., Zhou, X., Liu, C. and Zhang, X., 2017. Stepwise pH-responsive nanoparticles for enhanced cellular uptake and on-demand intracellular release of doxorubicin. *International Journal of Nanomedicine*, Volume 12, pp.4241-4256.

Danhier, F., 2016. To exploit the tumor microenvironment: Since the EPR effect fails in the clinic, what is the future of nanomedicine? *Journal of Controlled Release*, 244, pp.108-121.

Danquah, M., Zhang, X. and Mahato, R., 2011. Extravasation of polymeric nanomedicines across tumor vasculature. *Advanced Drug Delivery Reviews*, 63(8), pp.623-639.

Davis, M., Chen, Z. and Shin, D., 2008. Nanoparticle therapeutics: an emerging treatment modality for cancer. Nature Reviews *Drug Discovery*, 7(9), pp.771-782.

de Barros, A., Tsourkas, A., Saboury, B., Cardoso, V. and Alavi, A., 2012. Emerging role of radiolabeled nanoparticles as an effective diagnostic technique. *EJNMMI Research*, 2(1), p.39.

Denison, T. and Bae, Y., 2012. Tumor heterogeneity and its implication for drug delivery. *Journal of Controlled Release*, 164(2), pp.187-191.

De Simone, U., Roccio, M., Gribaldo, L., Spinillo, A., Caloni, F. and Coccini, T., 2018. Human 3D Cultures as Models for Evaluating Magnetic Nanoparticle CNS Cytotoxicity after Short- and Repeated Long-Term Exposure. *International Journal of Molecular Sciences*, 19(7), p.1993.

Dufau, I., Frongia, C., Sicard, F., Dedieu, L., Cordelier, P., Ausseil, F., Ducommun, B. and Valette, A., 2012. Multicellular tumor spheroid model to evaluate spatio-temporal dynamics effect of chemotherapeutics: application to the gemcitabine/CHK1 inhibitor combination in pancreatic cancer. *BMC Cancer*, 12(1).

Dvorak, H., Nagy, J., Dvorak, J. and Dvorak, A., 1988. Identification and characterization of the blood vessels of solid tumors that are leaky to circulating macromolecules. *American Journal of Pathology*, 133(1), pp.95-109.

Egusquiaguirre, S., Igartua, M., Hernández, R. and Pedraz, J., 2012. Nanoparticle delivery systems for cancer therapy: advances in clinical and preclinical research. *Clinical and Translational Oncology*, 14(2), pp.83-93.

Fan, Y., Du, W., He, B., Fu, F., Yuan, L., Wu, H., Dai, W., Zhang, H., Wang, X., Wang, J., Zhang, X. and Zhang, Q., 2013. The reduction of tumor interstitial fluid pressure by liposomal imatinib and its effect on combination therapy with liposomal doxorubicin. *Biomaterials*, 34(9), pp.2277-2288.

Faraji, A. and Wipf, P., 2009. Nanoparticles in cellular drug delivery. Bioorganic & *Medicinal Chemistry*, 17(8), pp.2950-2962.

Feng, D., Nagy, J., Dvorak, H. and Dvorak, A., 2002. Ultrastructural studies define soluble macromolecular, particulate, and cellular transendothelial cell pathways in venules, lymphatic vessels, and tumor-associated microvessels in man and animals. *Microscopy Research and Technique*, 57(5), pp.289-326.

Feng, D., Nagy, J., Hipp, J., Pyne, K., Dvorak, H. and Dvorak, A., 1997. Reinterpretation of endothelial cell gaps induced by vasoactive mediators in guinea-fig, mouse and rat: many are transcellular pores. *The Journal of Physiology*, 504(3), pp.747-761.

Feng, D., Nagy, J., Pyne, K., Hammel, I., Dvorak, H. and Dvorak, A., 1999. Pathways of Macromolecular Extravasation Across Microvascular Endothelium in Response to VPF/VEGF and Other Vasoactive Mediators. *Microcirculation*, 6(1), pp.23-44.

Feng, Y., Cheng, Y., Chang, Y., Jian, H., Zheng, R., Wu, X., Xu, K., Wang, L., Ma, X., Li, X. and Zhang, H., 2019. Time-staggered delivery of erlotinib and doxorubicin by gold nanocages with two smart polymers for reprogrammable release and synergistic with photothermal therapy. *Biomaterials*, 217, p.119327.

Frazier, N. and Ghandehari, H., 2015. Hyperthermia approaches for enhanced delivery of nanomedicines to solid tumors. *Biotechnology and Bioengineering*, 112(10), pp.1967-1983.

Gao, W., Chan, J. and Farokhzad, O., 2010. pH-Responsive Nanoparticles for Drug Delivery. *Molecular Pharmaceutics*, 7(6), pp.1913-1920.

Gatenby, R. and Gillies, R., 2004. Why do cancers have high aerobic glycolysis? *Nature Reviews Cancer*, 4(11), pp.891-899.

Ge, Z. and Liu, S., 2013. Functional block copolymer assemblies responsive to tumor and intracellular microenvironments for site-specific drug delivery and enhanced imaging performance. *Chemical Society Reviews*, 42(17), p.7289.

Haisler, W., Timm, D., Gage, J., Tseng, H., Killian, T. and Souza, G., 2013. Three-dimensional cell culturing by magnetic levitation. *Nature Protocols*, 8(10), pp.1940-1949.

Hatakeyama, H., Akita, H., Kogure, K., Oishi, M., Nagasaki, Y., Kihira, Y., Ueno, M., Kobayashi, H., Kikuchi, H. and Harashima, H., 2006. Development of a novel systemic gene delivery system for cancer therapy with a tumor-specific cleavable PEG-lipid. *Gene Therapy*, 14(1), pp.68-77.

He, X., Li, J., An, S. and Jiang, C., 2013. pH-sensitive drug-delivery systems for tumor targeting. *Therapeutic Delivery*, 4(12), pp.1499-1510.

He, Y., Su, Z., Xue, L., Xu, H. and Zhang, C., 2016. Co-delivery of erlotinib and doxorubicin by pH-sensitive charge conversion nanocarrier for synergistic therapy. *Journal of Controlled Release*, 229, pp.80-92.

Heldin, C., Rubin, K., Pietras, K. and Östman, A., 2004. High interstitial fluid pressure — an obstacle in cancer therapy. *Nature Reviews Cancer*, 4(10), pp.806-813.

Hirschhaeuser, F., Menne, H., Dittfeld, C., West, J., Mueller-Klieser, W. and Kunz-Schughart, L., 2010. Multicellular tumor spheroids: An underestimated tool is catching up again. *Journal of Biotechnology*, 148(1), pp.3-15.

Hobbs, S., Monsky, W., Yuan, F., Roberts, W., Griffith, L., Torchilin, V. and Jain, R., 1998. Regulation of transport pathways in tumor vessels: Role of tumor type and microenvironment. *Proceedings of the National Academy of Sciences*, 95(8), pp.4607-4612.

Horvath, P., Aulner, N., Bickle, M., Davies, A., Nery, E., Ebner, D., Montoya, M., Östling, P., Pietiäinen, V., Price, L., Shorte, S., Turcatti, G., von Schantz, C. and Carragher, N., 2016. Screening out irrelevant cell-based models of disease. *Nature Reviews Drug Discovery*, 15(11), pp.751-769.

Hoshyar, N., Gray, S., Han, H. and Bao, G., 2016. The effect of nanoparticle size on in vivo pharmacokinetics and cellular interaction. *Nanomedicine*, 11(6), pp.673-692.

Huber, K., Feuchtinger, A., Borgmann, D., Li, Z., Aichler, M., Hauck, S., Zitzelsberger, H., Schwaiger, M., Keller, U. and Walch, A., 2014. Novel Approach of MALDI Drug Imaging, Immunohistochemistry, and Digital Image Analysis for Drug Distribution Studies in Tissues. *Analytical Chemistry*, 86(21), pp.10568-10575.

Ishiyama, M., Tominaga, H., Shiga, M., Sasamoto, K., Ohkura, Y. and Ueno, K., 1996. A Combined Assay of Cell Viability and in Vitro Cytotoxicity with a Highly Water-Soluble Tetrazolium Salt, Neutral Red and Crystal Violet. *Biological & Pharmaceutical Bulletin*, 19(11), pp.1518-1520.

Jain, A. and Thareja, S., 2019. In vitro and in vivo characterization of pharmaceutical nanocarriers used for drug delivery. *Artificial Cells, Nanomedicine, and Biotechnology*, 47(1), pp.524-539.

Jain, R., 1999. Transport of Molecules, Particles, and Cells in Solid Tumors. *Annual Review of Biomedical Engineering*, 1(1), pp.241-263.

Jain, R. and Stylianopoulos, T., 2010. Delivering nanomedicine to solid tumors. *Nature Reviews Clinical Oncology*, 7(11), pp.653-664.

Junttila, M. and de Sauvage, F., 2013. Influence of tumour micro-environment heterogeneity on therapeutic response. *Nature*, 501(7467), pp.346-354.

Keereweer, S., Van Driel, P., Snoeks, T., Kerrebijn, J., Baatenburg de Jong, R., Vahrmeijer, A., Sterenborg, H. and Lowik, C., 2013. Optical Image-Guided Cancer Surgery: Challenges and Limitations. *Clinical Cancer Research*, 19(14), pp.3745-3754.

Kell, D. and Oliver, S., 2014. How drugs get into cells: tested and testable predictions to help discriminate between transporter-mediated uptake and lipoidal bilayer diffusion. *Frontiers in Pharmacology*, 5.

Kelm, J., Timmins, N., Brown, C., Fussenegger, M. and Nielsen, L., 2003. Method for generation of homogeneous multicellular tumor spheroids applicable to a wide variety of cell types. *Biotechnology and Bioengineering*, 83(2), pp.173-180.

Kohli, A., Kivimäe, S., Tiffany, M. and Szoka, F., 2014. Improving the distribution of Doxil® in the tumor matrix by depletion of tumor hyaluronan. *Journal of Controlled Release*, 191, pp.105-114.

Kong, B., Seog, J., Graham, L. and Lee, S., 2011. Experimental considerations on the cytotoxicity of nanoparticles. *Nanomedicine*, 6(5), pp.929-941.

Kulkarni, S. and Feng, S., 2013. Effects of Particle Size and Surface Modification on Cellular Uptake and Biodistribution of Polymeric Nanoparticles for Drug Delivery. *Pharmaceutical Research*, 30(10), pp.2512-2522.

Lammers, T., Kiessling, F., Hennink, W. and Storm, G., 2012. Drug targeting to tumors: Principles, pitfalls and (pre-) clinical progress. *Journal of Controlled Release*, 161(2), pp.175-187.

Lee, E., Gao, Z. and Bae, Y., 2008. Recent progress in tumor pH targeting nanotechnology. *Journal of Controlled Release*, 132(3), pp.164-170.

Lee, J., Lilly, G., Doty, R., Podsiadlo, P. and Kotov, N., 2009. In vitro Toxicity Testing of Nanoparticles in 3D Cell Culture. *Small*, p.NA-NA.

Lee, M., Ye, A., Gardino, A., Heijink, A., Sorger, P., MacBeath, G. and Yaffe, M., 2012. Sequential Application of Anticancer Drugs Enhances Cell Death by Rewiring Apoptotic Signaling Networks. *Cell*, 149(4), pp.780-794.

Li, L., Sun, W., Zhong, J., Yang, Q., Zhu, X., Zhou, Z., Zhang, Z. and Huang, Y., 2015. Multistage Nanovehicle Delivery System Based on Stepwise Size Reduction and Charge Reversal for Programmed Nuclear Targeting of Systemically Administered Anticancer Drugs. *Advanced Functional Materials*, 25(26), pp.4101-4113.

Li, S. and Huang, L., 2009. Nanoparticles evading the reticuloendothelial system: Role of the supported bilayer. *Biochimica et Biophysica Acta (BBA) - Biomembranes*, 1788(10), pp.2259-2266.

Li, Y., Yang, J., Xu, B., Gao, F., Wang, W. and Liu, W., 2015. Enhanced Therapeutic siRNA to Tumor Cells by a pH-Sensitive Agmatine–Chitosan Bioconjugate. *ACS Applied Materials & Interfaces*, 7(15), pp.8114-8124.

Liu, J., Huang, Y., Kumar, A., Tan, A., Jin, S., Mozhi, A. and Liang, X., 2014. pH-Sensitive nano-systems for drug delivery in cancer therapy. *Biotechnology Advances*, 32(4), pp.693-710.

Ma, S., Nishikawa, M., Katsumi, H., Yamashita, F. and Hashida, M., 2005. Cationic charge-dependent hepatic delivery of amidated serum albumin. *Journal of Controlled Release*, 102(3), pp.583-594.

Matsumura, Y. and Maeda, H., 1986. A New Concept for Macromolecular Therapeutics in Cancer Chemotherapy: Mechanism of Tumoritropic Accumulation of Proteins and the Antitumor Agent Smancs. *Cancer Research*, 12(1), pp.6387-6392.

McDonald, D., 1999. Uptake of Cationic Liposomes by Normal and Angiogenic Endothelial Cells In Vivo. *Nature Biotechnology*, 17(S4), pp.14-14.

McDonald, D., Thurston, G. and Baluk, P., 1999. Endothelial Gaps as Sites for Plasma Leakage in Inflammation. *Microcirculation*, 6(1), pp.7-22.

Miao, L., Lin, C. and Huang, L., 2015. Stromal barriers and strategies for the delivery of nanomedicine to desmoplastic tumors. *Journal of Controlled Release*, 219, pp.192-204.

Michel, C. and Neal, C., 1999. Openings Through Endothelial Cells Associated with Increased Microvascular Permeability. *Microcirculation*, 6(1), pp.45-54.

Mittler, F., Obeïd, P., Rulina, A., Haguet, V., Gidrol, X. and Balakirev, M., 2017. High-Content Monitoring of Drug Effects in a 3D Spheroid Model. *Frontiers in Oncology*, 7.

Mo, R., Sun, Q., Li, N. and Zhang, C., 2013. Intracellular delivery and antitumor effects of pH-sensitive liposomes based on zwitterionic oligopeptide lipids. *Biomaterials*, 34(11), pp.2773-2786.

Moghimi, S., Hunter, A. and Andresen, T., 2012. Factors Controlling Nanoparticle Pharmacokinetics: An Integrated Analysis and Perspective. *Annual Review of Pharmacology and Toxicology*, 52(1), pp.481-503.

Morton, S., Lee, M., Deng, Z., Dreaden, E., Siouve, E., Shopsowitz, K., Shah, N., Yaffe, M. and Hammond, P., 2014. A Nanoparticle-Based Combination Chemotherapy Delivery System for Enhanced Tumor Killing by Dynamic Rewiring of Signaling Pathways. *Science Signaling*, 7(325), pp.ra44-ra44.

Nagy, J., Feng, D., Vasile, E., Wong, W., Shih, S., Dvorak, A. and Dvorak, H., 2006. Permeability properties of tumor surrogate blood vessels induced by VEGF-A. *Laboratory Investigation*, 86(8), pp.767-780.

Nath, S. and Devi, G., 2016. Three-dimensional culture systems in cancer research: Focus on tumor spheroid model. *Pharmacology & Therapeutics*, 163, pp.94-108.

Neal, C. and Michel, C., 1997. Transcellular openings through frog microvascular endothelium. *Experimental Physiology*, 82(2), pp.419-422.

Nesargikar, P., Spiller, B. and Chavez, R., 2012. The complement system: History, pathways, cascade and inhibitors. *European Journal of Microbiology and Immunology*, 2(2), pp.103-111.

Nichols, J. and Bae, Y., 2014. EPR: Evidence and fallacy. *Journal of Controlled Release*, 190, pp.451-464.

Nie, S., 2010. Understanding and overcoming major barriers in cancer nanomedicine. *Nanomedicine*, 5(4), pp.523-528.

O'Brien, M., Wigler, N., Inbar, M., Rosso, R., Grischke, E., Santoro, A., Catane, R., Kieback, D., Tomczak, P., Ackland, S., Orlandi, F., Mellars, L., Alland, L. and Tendler, C., 2004. Reduced cardiotoxicity and comparable efficacy in a phase III trial of pegylated liposomal doxorubicin HCl (CAELYXTM/Doxil") versus conventional doxorubicin for first-line treatment of metastatic breast cancer. *Annals of Oncology*, 15(3), pp.440-449.

Oh, P., Testa, J., Borgstrom, P., Witkiewicz, H., Li, Y. and Schnitzer, J., 2014. In vivo proteomic imaging analysis of caveolae reveals pumping system to penetrate solid tumors. *Nature Medicine*, 20(9), pp.1062-1068.

Ooi, Y., Wen, Y., Zhu, J., Song, X. and Li, J., 2020. Surface Charge Switchable Polymer/DNA Nanoparticles Responsive to Tumor Extracellular pH for Tumor-Triggered Enhanced Gene Delivery. *Biomacromolecules*, 21(3), pp.1136-1148.

Padera, T., Kadambi, A., Tomaso, E., Carreira, C., Brown, E., Boucher, Y., Choi, N., Mathisen, D., Wain, J., Mark, E., Munn, L. and Jain, R., 2002. Lymphatic Metastasis in the Absence of Functional Intratumor Lymphatics. *Science*, 296(5574), pp.1883-1886.

Patra, J., Das, G., Fraceto, L., Campos, E., Rodriguez-Torres, M., Acosta-Torres, L., Diaz-Torres, L., Grillo, R., Swamy, M., Sharma, S., Habtemariam, S. and Shin, H., 2018. Nano based drug delivery systems: recent developments and future prospects. *Journal of Nanobiotechnology*, 16(1).

Perez, J., Fuertes, M., Nguewa, P., Castilla, J. and Alonso, C., 2008. Anticancer Compounds as Leishmanicidal Drugs: Challenges in Chemotherapy and Future Perspectives. *Current Medicinal Chemistry*, 15(5), pp.433-439.

Prabhakar, U., Maeda, H., Jain, R., Sevick-Muraca, E., Zamboni, W., Farokhzad, O., Barry, S., Gabizon, A., Grodzinski, P. and Blakey, D., 2013. Challenges and Key Considerations of the Enhanced Permeability and Retention Effect for Nanomedicine Drug Delivery in Oncology. *Cancer Research*, 73(8), pp.2412-2417.

Primeau, A., Rendon, A., Hedley, D., Lilge, L., and Tannock, I.F., 2005. The Distribution of the Anticancer Drug Doxorubicin in Relation to Blood Vessels in Solid Tumors. *Clinical Cancer Research*, 11(24), pp.8782-8788.

Rajabi, M. and Mousa, S., 2017. The Role of Angiogenesis in Cancer Treatment. *Biomedicines*, 5(4), p.34.

Risau, W., 1997. Mechanisms of angiogenesis. *Nature*, 386(6626), pp.671-674.

Riaz, M., Riaz, M., Zhang, X., Lin, C., Wong, K., Chen, X., Zhang, G., Lu, A. and Yang, Z., 2018. Surface Functionalization and Targeting Strategies of Liposomes in Solid Tumor Therapy: A Review. *International Journal of Molecular Sciences*, 19(1), p.195.

Ross, R., Paganini-Hill, A., Wan, P. and Pike, M., 2000. Effect of Hormone Replacement Therapy on Breast Cancer Risk: Estrogen Versus Estrogen Plus Progestin. *Journal of the National Cancer Institute*, 92(4), pp.328-332.

Salatin, S. and Khosroushahi, A., 2017. Overviews on the cellular uptake mechanism of polysaccharide colloidal nanoparticles. *Journal of Cellular and Molecular Medicine*, 21(9), pp.1668-1686.

Sambi, M., Bagheri, L. and Szewczuk, M., 2019. Current Challenges in Cancer Immunotherapy: Multimodal Approaches to Improve Efficacy and Patient Response Rates. *Journal of Oncology*, 2019, pp.1-12.

Scannell, J., Blanckley, A., Boldon, H. and Warrington, B., 2012. Diagnosing the decline in pharmaceutical R&D efficiency. *Nature Reviews Drug Discovery*, 11(3), pp.191-200.

Schaue, D. and McBride, W., 2015. Opportunities and challenges of radiotherapy for treating cancer. *Nature Reviews Clinical Oncology*, 12(9), pp.527-540.

Schnitzer, J., 1992. gp60 is an albumin-binding glycoprotein expressed by continuous endothelium involved in albumin transcytosis. *American Journal of Physiology-Heart and Circulatory Physiology*, 262(1), pp.H246-H254.

Sindhwani, S., Syed, A., Ngai, J., Kingston, B., Maiorino, L., Rothschild, J., MacMillan, P., Zhang, Y., Rajesh, N., Hoang, T., Wu, J., Wilhelm, S., Zilman, A., Gadde, S., Sulaiman, A., Ouyang, B., Lin, Z., Wang, L., Egeblad, M. and Chan, W., 2020. The entry of nanoparticles into solid tumours. *Nature Materials*.

Smith, L., Watson, M., O'Kane, S., Drew, P., Lind, M. and Cawkwell, L., 2006. The analysis of doxorubicin resistance in human breast cancer cells using antibody microarrays. *Molecular Cancer Therapeutics*, 5(8), pp.2115-2120.

Smyrek, I. and Stelzer, E., 2017. Quantitative three-dimensional evaluation of immunofluorescence staining for large whole mount spheroids with light sheet microscopy. *Biomedical Optics Express*, 8(2), p.484.

Soo Choi, H., Liu, W., Misra, P., Tanaka, E., Zimmer, J., Itty Ipe, B., Bawendi, M. and Frangioni, J., 2007. Renal clearance of quantum dots. *Nature Biotechnology*, 25(10), pp.1165-1170.

Sperling, R. and Parak, W., 2010. Surface modification, functionalization and bioconjugation of colloidal inorganic nanoparticles. Philosophical Transactions of the Royal Society A: Mathematical, *Physical and Engineering Sciences*, 368(1915), pp.1333-1383.

Statistics Canada. 2020. *Leading Causes Of Death, Total Population, By Age Group*. [online] Available at: <https://www150.statcan.gc.ca/t1/tbl1/en/tv.action?pid=1310039401> [Accessed 2 March 2020].

Stone, V., Johnston, H. and Schins, R., 2009. Development of in vitro systems for nanotoxicology: methodological considerations. *Critical Reviews in Toxicology*, 39(7), pp.613-626.

Strober, W., 2015. Trypan Blue Exclusion Test of Cell Viability. *Current Protocols in Immunology*, 111(1).

Svedberg, A., Gréen, H., Vikström, A., Lundeberg, J. and Vikingsson, S., 2015. A validated liquid chromatography tandem mass spectrometry method for quantification of erlotinib, OSI-420 and didesmethyl erlotinib and semi-quantification of erlotinib metabolites in human plasma. *Journal of Pharmaceutical and Biomedical Analysis*, 107, pp.186-195.

Tchoryk, A., Taresco, V., Argent, R., Ashford, M., Gellert, P., Stolnik, S., Grabowska, A. and Garnett, M., 2019. Penetration and Uptake of Nanoparticles in 3D Tumor Spheroids. *Bioconjugate Chemistry*, 30(5), pp.1371-1384.

Thoma, C., Zimmermann, M., Agarkova, I., Kelm, J. and Krek, W., 2014. 3D cell culture systems modeling tumor growth determinants in cancer target discovery. *Advanced Drug Delivery Reviews*, 69-70, pp.29-41.

Thurston, G., McLean, J., Rizen, M., Baluk, P., Haskell, A., Murphy, T., Hanahan, D. and McDonald, D., 1998. Cationic liposomes target angiogenic endothelial cells in tumors and chronic inflammation in mice. *Journal of Clinical Investigation*, 101(7), pp.1401-1413.

Vander Heiden, M., Cantley, L. and Thompson, C., 2009. Understanding the Warburg Effect: The Metabolic Requirements of Cell Proliferation. *Science*, 324(5930), pp.1029-1033.

Vinci, M., Box, C. and Eccles, S., 2015. Three-Dimensional (3D) Tumor Spheroid Invasion Assay. *Journal of Visualized Experiments*, (99).

Vinci, M., Gowan, S., Boxall, F., Patterson, L., Zimmermann, M., Court, W., Lomas, C., Mendiola, M., Hardisson, D. and Eccles, S., 2012. Advances in establishment and analysis of three-dimensional tumor spheroid-based functional assays for target validation and drug evaluation. *BMC Biology*, 10(1), p.29.

Wagner, V., Dullaart, A., Bock, A. and Zweck, A., 2006. The emerging nanomedicine landscape. *Nature Biotechnology*, 24(10), pp.1211-1217.

Wang, J., Lu, Z., Wang, J., Cui, M., Yeung, B., Cole, D., Wientjes, M. and Au, J., 2015a. Paclitaxel tumor priming promotes delivery and transfection of intravenous lipid-siRNA in pancreatic tumors. *Journal of Controlled Release*, 216, pp.103-110.

Wang, J., Mao, W., Lock, L., Tang, J., Sui, M., Sun, W., Cui, H., Xu, D. and Shen, Y., 2015b. The Role of Micelle Size in Tumor Accumulation, Penetration, and Treatment. *ACS Nano*, 9(7), pp.7195-7206.

Weiswald, L., Bellet, D. and Dangles-Marie, V., 2015. Spherical Cancer Models in Tumor Biology. *Neoplasia*, 17(1), pp.1-15.

Weiswald, L., Guinebretière, J., Richon, S., Bellet, D., Saubaméa, B. and Dangles-Marie, V., 2010. In situ protein expression in tumour spheres: development of an immunostaining protocol for confocal microscopy. *BMC Cancer*, 10(1).

World Health Organization. 2018. *Cancer*. [online] Available at: <https://www.who.int/news-room/fact-sheets/detail/cancer> [Accessed 21 January 2019].

Zhang, W., Siu, L., Moore, M. and Chen, E., 2005. Simultaneous determination of OSI-774 and its major metabolite OSI-420 in human plasma by using HPLC with UV detection. *Journal of Chromatography B*, 814(1), pp.143-147.

Zanoni, M., Piccinini, F., Arienti, C., Zamagni, A., Santi, S., Polico, R., Bevilacqua, A. and Tesei, A., 2016. 3D tumor spheroid models for in vitro therapeutic screening: a systematic approach to enhance the biological relevance of data obtained. *Scientific Reports*, 6(1).

Zhao, Z., Meng, H., Wang, N., Donovan, M., Fu, T., You, M., Chen, Z., Zhang, X. and Tan, W., 2013. A Controlled-Release Nanocarrier with Extracellular pH Value Driven Tumor Targeting and Translocation for Drug Delivery. *Angewandte Chemie International Edition*, 52(29), pp.7487-7491.

Zhou, M., Huang, H., Wang, D., Lu, H., Chen, J., Chai, Z., Yao, S. and Hu, Y., 2019. Light-Triggered PEGylation/dePEGylation of the Nanocarriers for Enhanced Tumor Penetration. *Nano Letters*, 19(6), pp.3671-3675.

Zhou, Q., Zhang, L., Yang, T. and Wu, H., 2018. Stimuli-responsive polymeric micelles for drug delivery and cancer therapy. *International Journal of Nanomedicine*, Volume 13, pp.2921-2942.

Supplementary Figures

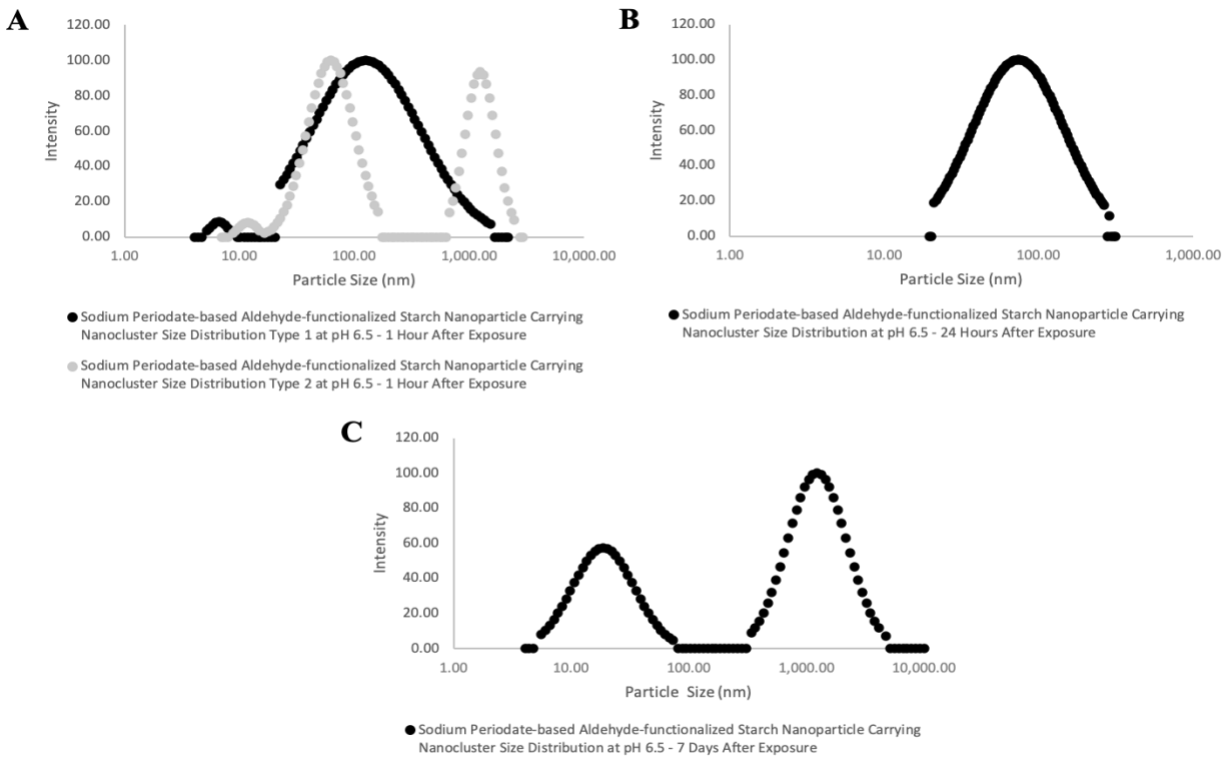

Supplementary Figure 1: DLS number average size distributions of $NaIO_4$-based Ald-SNP carrying nanoclusters in acidic conditions over time. (A) Nanocluster DLS readings 1 hour after exposure to acidic conditions. (B) Nanocluster DLS readings 24 hours after exposure to acidic conditions. (C) Nanocluster DLS readings 7 days after exposure to acidic conditions. Peaks of around 90-100 nm represent nanoclusters, peaks around 20 nm represent released Ald-SNPs (corresponding to nanocluster disassembly), and peaks around 1000 nm represent nanocluster and polymer aggregates.

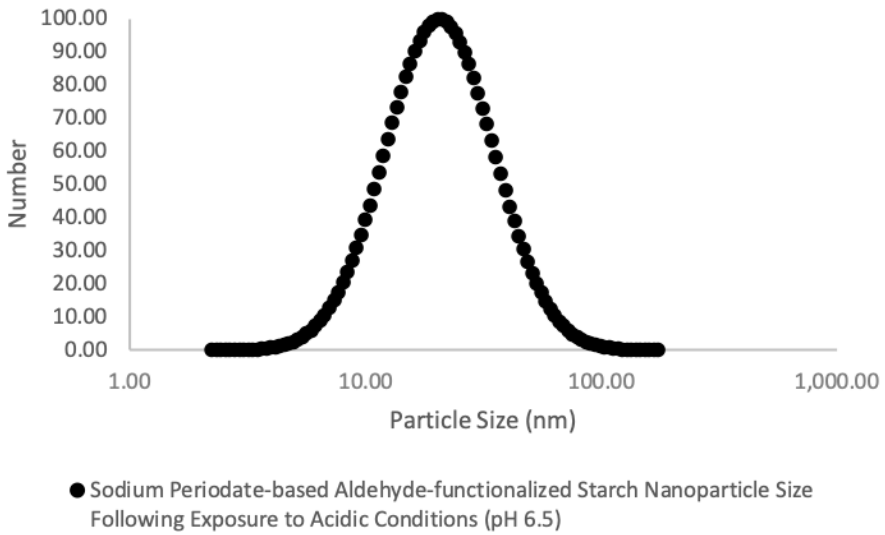

Supplementary Figure 2: DLS number average size distributions of $NaIO_4$-based Ald-SNPs following exposure to acidic conditions (pH 6.5).

Supplementary Table 1: Overview of $NaIO_3$-based Ald-SNP carrying nanocluster DLS and zeta potential readings over time under neutral (pH 7) conditions.

Sample	Mean Particle size (nm)	Standard Deviation (nm)	Polydispersity	Zeta Potential (mV)
Nanoclusters – 1 Day After Formation	67	2.44	0.262	0.50
Nanoclusters – 5 Days After Formation	64	2.84	0.232	0.55

Supplementary Table 2: Overview of $NaIO_3$-based Ald-SNP carrying nanocluster DLS and zeta potential readings over time under acidic (pH 6.5) conditions.

Sample	Mean Particle size (nm)	Standard Deviation (nm)	Polydispersity	Zeta Potential (mV)
Nanoclusters – 1 Hour After Exposure	10,702	25,676.64	0.431	3
Nanoclusters – 1 Day After Exposure	32,606	52.873.33	0.444	1